Journal of Solid State Chemistry **148,** 380–405 (1999)
Article ID jssc.1999.8467, available online at http://www.idealibrary.com on IDEAL®

Structural Relationships among Bismuth-Rich Phases in the Bi_2O_3–Nb_2O_5, Bi_2O_3–Ta_2O_5, Bi_2O_3–MoO_3, and Bi_2O_3–WO_3 Systems

Christopher D. Ling[1]

Research School of Chemistry, Australian National University, Canberra, ACT 0200, Australia

Received April 28, 1999; in revised form July 28, 1999; accepted August 10, 1999

The crystal structures of bismuth-rich phases in the Bi_2O_3–M_2O_5 (M = Nb, Ta) and Bi_2O_3–M_2O_6 (M = W, Mo) systems are investigated, and the most probable model for the crystal structure of each phase is used to propose a crystal–chemical scheme unifying key features of these structures in terms of their relationships to a fluorite-type δ-Bi_2O_3-related parent structure. This scheme is based on the incorporation of pyrochlore-type structural motifs (e.g., strings of M atoms along $\langle 1\,1\,0\rangle_F$ directions) into the underlying fluorite-type metal atom array. The relative orientations of these M atom strings and their interactions are driven by the competing requirements of overall charge-balance (a function of mol% M_2O_5 or M_2O_6) and local coordination environment (a function of the element M) within the flexible fluorite-type oxygen atom array. These interactions interrelate the oxygen atom array, the metal atom array, and the composition. As the composition moves further from pure Bi_2O_3, they force the abandonment of pyrochlore-type structural motifs, and hence any meaningful relationship to a fluorite-type δ-Bi_2O_3-related parent structure is lost. The descriptive and predictive utilities of this crystal–chemical scheme are discussed. © 1999 Academic Press

INTRODUCTION

This study concerns the Bi_2O_3-rich ends of the pseudo-binary systems Bi_2O_3–Nb_2O_5, Bi_2O_3–Ta_2O_5, Bi_2O_3–WO_3, and Bi_2O_3–MoO_3. Interest in these particular systems stems from the high-temperature form of bismuth oxide, δ-Bi_2O_3, one of the best solid-state oxygen ion conductors known (1, 2). Bismuth oxide is strongly polymorphic (α-, β-, γ-, and δ-forms are known) (3) and pure δ-Bi_2O_3 cannot be quenched to room temperature. However, certain transition metal oxides (including those listed above), when added to Bi_2O_3 as the minor component, are known to form phases which often preserve a structure related to that of δ-Bi_2O_3 and retain much of its anionic conduction properties. This study therefore focuses on δ-Bi_2O_3-related phases found at the bismuth-rich ends of the respective phase diagrams.

δ-Bi_2O_3 itself has an approximately face-centered cubic (fcc) structure akin to that of fluorite (CaF_2) with an average oxygen occupancy of 75% (3, 4) (Fig. 1). The metal atoms thus form an fcc cation array with oxygen atoms (at the 75% level) occupying the tetrahedral sites therein. The oxygen vacancies in this model are supposed to account for its ionic conduction properties. Battle *et al.* (5) have refined a disordered variant of this model, in which 43% of the oxygen atoms move $\sim$1 Å from the exact tetrahedral site along $\langle 1\,1\,1\rangle_F$ directions.

The disordered average coordination environment of bismuth atoms within this fluorite-type model for δ-Bi_2O_3 (cubic, with 75% occupancy of each site) (Fig. 1) and its oxygen ion conductivity imply that the actual local coordination environments of bismuth atoms must be highly variable. This flexibility in the oxygen atom array means that when considering the relationships to fluorite-type of individual phases, it is appropriate to consider the metal atom array before the oxygen atom array.

X-ray powder diffraction (XRD) and transmission electron microscopy (both high-resolution (HRTEM) and electron diffraction (ED)), techniques most sensitive to the metal atom array, often appeared to indicate that the phases with which this study is concerned do form modulated variants of a fluorite-type δ-Bi_2O_3 structure (6–17). This implied that the structures should be characterized most succinctly by an underlying fluorite-type δ-Bi_2O_3-related average structure plus compositional and/or displacive modulations thereof. The extent to which each phase could be meaningfully described as a modulated variant of δ-Bi_2O_3 was considered in a recent study (18).

The observation of satellite reflections in addition to the strong Bragg reflections of an underlying δ-Bi_2O_3-related average structure (or at least fcc cation array) usually indicates the presence of metal atom compositional ordering. The question of whether, and to what extent, this is accompanied by oxygen vacancy ordering and displacing relaxation of the remaining oxygen atoms has a strong bearing

[1] Present address: Materials Science Division, Argonne National Laboratory, Argonne, IL 60439.

0022-4596/99 $30.00

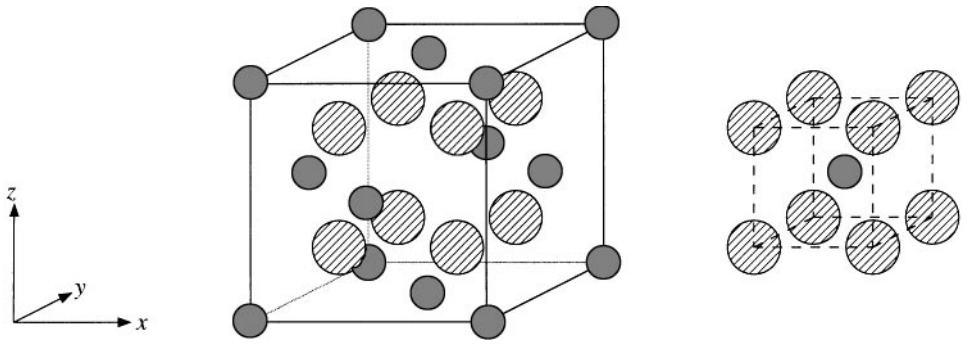

FIG. 1. The average fluorite-type structure of δ-Bi_2O_3 ($Fm3m$, $a = 5.6595(4)$ Å) showing the average cubic coordination environment (dashed lines) of bismuth atoms (dark gray). Oxygen sites (striped) are 75% occupied.

on the level of detail to which the structures of individual phases can be determined by diffraction methods. In a series of very recent structural studies (19), it was found that when oxygen atoms were fully ordered, and useful single crystals could be grown, it was possible to obtain complete structural solutions (20, 21). When, however, the oxygen atoms were only partially ordered, determining chemically and crystallographically satisfactory structural solutions proved to be extremely difficult (22, 23).

The highly polymorphic nature of bismuth oxide itself, in conjunction with the ability of small proportions of transition metal atoms to influence the structure type adopted, clearly indicates that these δ-Bi_2O_3-related structures are the result of a delicate balance of competing crystal chemical interactions. The structure type adopted by a given phase will be a function of the interaction between the ability of Bi^{3+} to adopt a variety of coordination environments and the tendency of the transition metal cations to adopt more rigidly defined octahedral or tetrahedral coordination environments. In order to understand these phases it will be necessary to understand the relationship between the concentration of the transition metal atoms and the structure types adopted; this relationship, and the interactions that govern it, may be played out within the context of a unifying crystal chemical scheme.

Such a unifying crystal chemical scheme might well be based upon the incorporation of pyrochlore-type structural motifs into an underlying fluorite-type average structure, following the use by Zhou *et al.* (8–16) of a pyrochlore-type structural motif in modeling some of these phases. (The pyrochlore-type structure, ideal stoichiometry $A_2B_2O_7$, can be described as a $2 \times 2 \times 2$ metal atom ordered fluorite-type superstructure phase (24).) In these models, transition metal atoms condense in tetrahedra of nearest-neighbor metal atoms within the fcc fluorite-type metal atom array. When the transition metal atoms prefer octahedral coordination environments, an ordered pattern of fluorite-type oxygen vacancies follows this metal atom compositional ordering pattern (Fig. 2a), creating a tetrahedron of (somewhat distorted) octahedra (Fig. 2b). Oxygen atom displacements from fluorite-type positions obviously follow, in order to satisfy chemical bonding requirements. In pyrochlore-type itself, these tetrahedral metal atom clusters (Fig. 2c) are infinitely corner-connected as shown in Fig. 2d. A scheme built around this motif could therefore provide a framework within which to model metal atom compositional ordering, and subsequently oxygen vacancy ordering and oxygen atom displacements, from a fluorite-type δ-Bi_2O_3 archetype.

Zhou *et al.* (8–16) also used a labeling scheme for the phases they investigated, based on HRTEM and ED data and therefore complimenting their structural models proposed on the basis of that data. For clarity, the same labeling scheme (including Types I–IV, Ia, Ib, and II*) is used in the present study.

The "tetrahedra of octahedra" used by Zhou *et al.* are in fact only one of several structural motifs which can be identified in pyrochlore-type, any of which could form the basis of a crystal–chemical scheme incorporating pyrochlore-type structural motifs into a fluorite-type average structure. Figure 3a shows the B_2O_6 array in pyrochlore-type $A_2B_2O_7$, from which a variety of structural motifs can be drawn, including isolated BO_6 octahedra (Fig. 3b), B_4O_{18} tetrahedra of BO_6 octahedra (Fig. 3c), and B_nO_{5n+1} strings of n corner-connected BO_6 octahedra (Fig. 3*d*). Potential crystal chemical schemes based on all such motifs are considered in this study.

The success or otherwise of this study depends critically on the accumulation of sufficient data. The most probable structure for each phase will therefore be considered, including (tentatively) some relatively poorly resolved structures (19) alongside well-resolved structures (20–23). (It must be emphasised that the former are being advanced not as exact solutions but in order to further the construction of a unifying crystal–chemical scheme. It is hoped that this scheme will assist in finding more definitive solutions of the same structures, if and when better diffraction data is obtained.) Given their demonstrated relationship to the Type

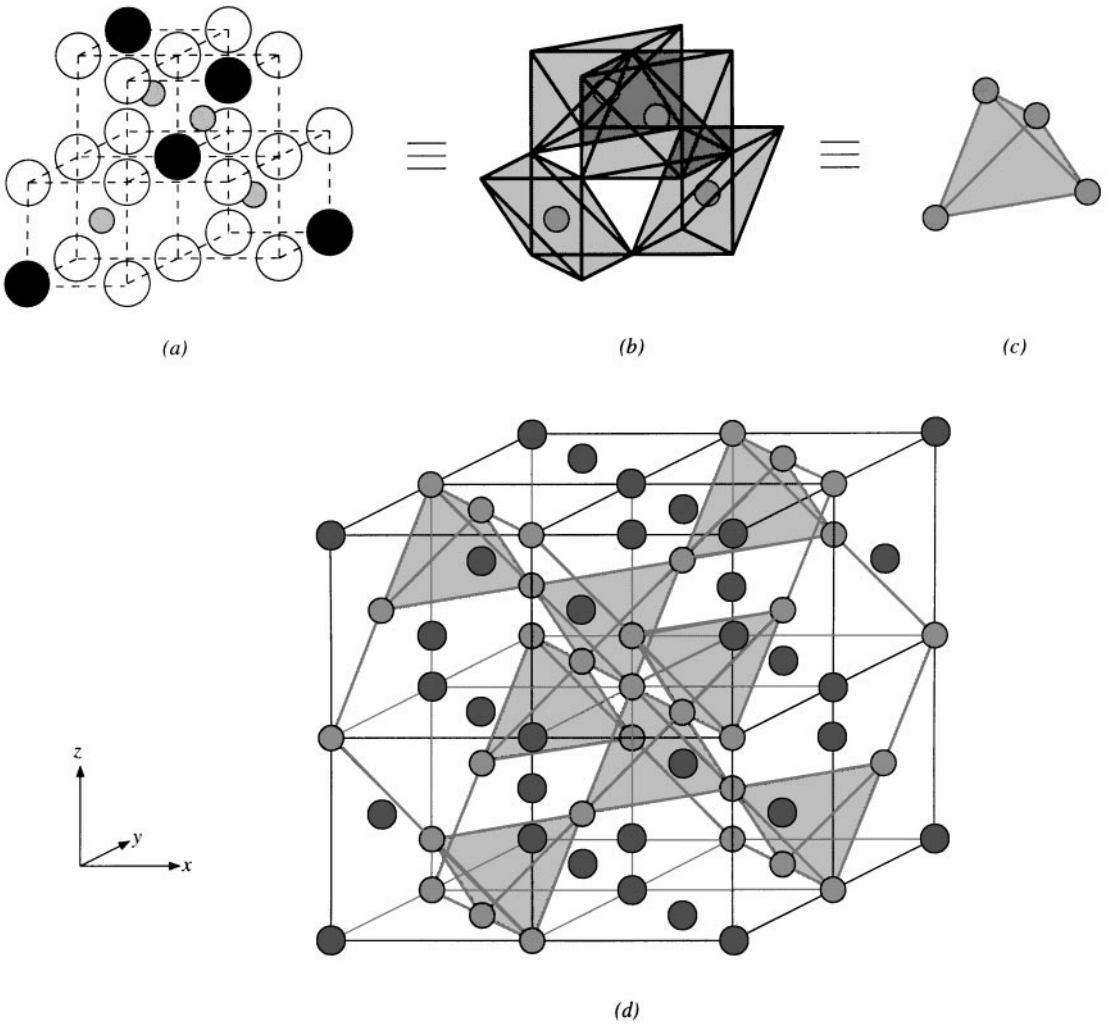

FIG. 2. Scheme for the incorporation of a pyrochlore-type structural motif into a fluorite-type average structure. (a) The arrangement of vacancies (black) within the fluorite-type oxygen lattice (white) surrounding a tetrahedron of transition metal atoms (light gray). This reduces the cubic coordination of metal atoms in fluorite-type (dashed lines) to octahedral coordination (b) (oxygen atom displacing relaxations are not shown). These tetrahedral clusters (c) are then infinitely corner-connected in pyrochlore-type itself (d).

IV phases (6, 8, 12, 18, 19), the $n = 1$ Aurivillius phases Bi_2WO_6 and γ-Bi_2MoO_6 (25) have also been added to the data pool for consideration. Finally, phases whose space groups and unit cells approximate higher symmetry space groups and unit cells will be considered in terms of those high-symmetry approximates (18). This is in order to focus attention on the general structural principles that certain phases have in common, rather than on the small-scale perturbations which differentiate them.

STRUCTURAL MODELS

Bi_2O_3–Ta_2O_5 Type I

$Bi_{15}TaO_{25}$, the Type I phase in the Bi_2O_3–Ta_2O_5 system, is a cubic $2 \times 2 \times 2$, *I*-centered superstructure of fluorite-type (14, 18). There is therefore only one possible (fully ordered) Bi/Ta metal atom compositional ordering scheme, as shown in Fig. 4 and as originally proposed by Zhou *et al.* (14). Ta atoms in this scheme have the maximum possible separation from one another. The model has *Im*3*m* space group symmetry. If the assumption is made that Ta atoms are in octahedral coordination environments, then there are two fluorite-type oxygen vacancies associated with each Ta atom, giving the stoichiometry $Bi_{15}TaO_{30}$. There must therefore be five additional fluorite-type oxygen vacancies associated with Bi atoms only.

Synchrotron XRD satellite reflection intensities were too weak to be used to test this model. An XRD pattern calculated on the basis of the model shown in Fig. 4 identified the most intense satellite reflection [(1 1 0)*] as having

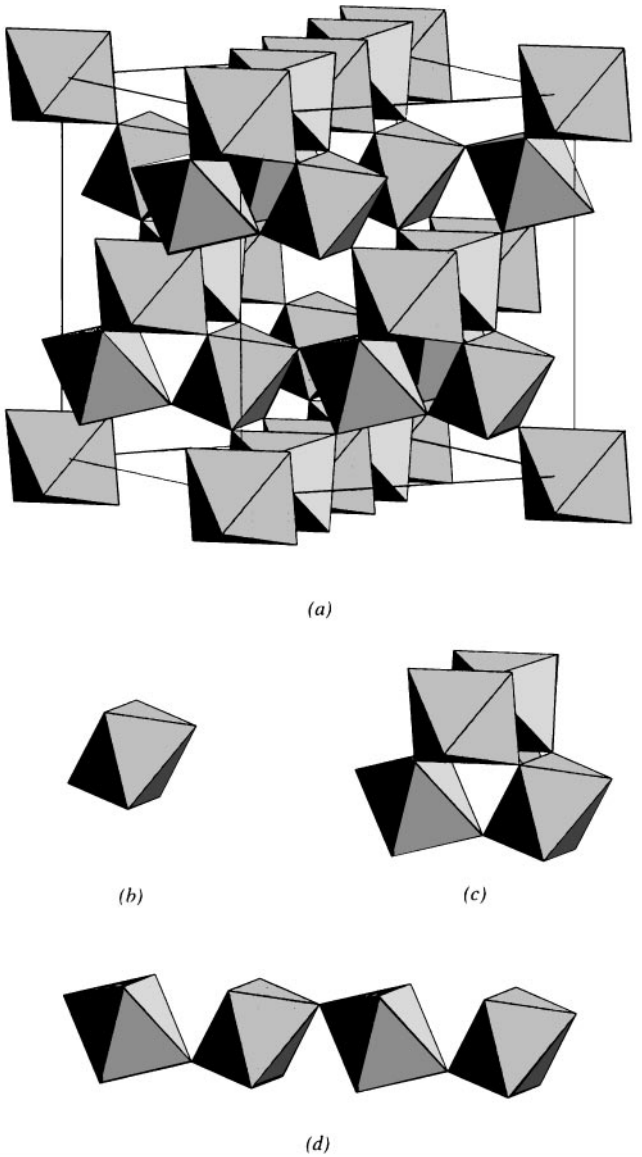

FIG. 3. (a) The B_2O_6 array in ideal pyrochlore-type $A_2B_2O_7$, and some of the structural motifs that can be drawn from it, (b) isolated BO_6 octahedra, (c) B_4O_{18} tetrahedra of BO_6 octahedra, and (d) B_nO_{5n+1} strings of n corner-connected BO_6 octahedra.

only 0.1% the intensity of the strongest reflection, $(2\,2\,2)^* \equiv (1\,1\,1)^*_F$. The weakness of the satellite reflections in XRD requires that there be negligible displacing relaxation of the metal atom array from fluorite-type positions. Neutron powder diffraction data were required to determine whether oxygen vacancy ordering was also occurring. In the absence of any contradictory evidence, it must be concluded that the Bi/Ta metal atom ordering scheme shown in Fig. 4 is the simplest, highest symmetry, and most probable solution for the metal atom array of $Bi_{15}TaO_{25}$.

Bi_2O_3–WO_3 and Bi_2O_3–MoO_3 Type Ia

The structure of Type Ia $Bi_{14}(W/Mo)O_{24}$ has been recently solved and refined using neutron powder diffraction data in the space group $I4/m$ (20) (Fig. 5). The metal atom array is fully ordered and deviates only slightly from a fluorite-type δ-Bi_2O_3-related parent structure. Three independent oxygen atom sites (accounting for 70 out of 78 oxygen atoms in the unit cell) are also very close to fluorite-type parent positions. The remaining two oxygen atom sites coordinate the W/Mo atom and exhibit partial occupancies and displacive disorder, neither of which were better modeled through symmetry lowering. The W/Mo atom is in fact coordinated by four oxygen atoms in highly distorted tetrahedral coordination, the tetrahedron necessarily being orientationally disordered on that site. The structure appears to be chemically reasonable.

Bi_2O_3–WO_3 Type Ib

The Type Ib phase in the Bi_2O_3–WO_3 system is a solid-solution with metal atom compositions between approximately 12.5 and 16.0 mol% W_2O_6. Recent ED work (18) supported previous descriptions (15, 26) of the phase as a superstructure of fluorite-type and indicated the space

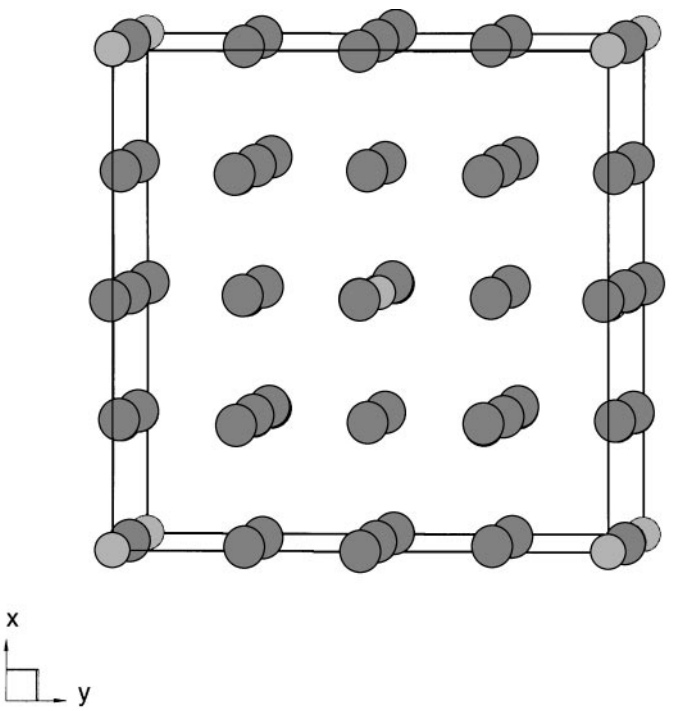

FIG. 4. The (unrefined) metal atom ordering model for Type I $Bi_{15}TaO_{25}$ (14, 19). Bismuth atoms are darker than tantalum atoms.

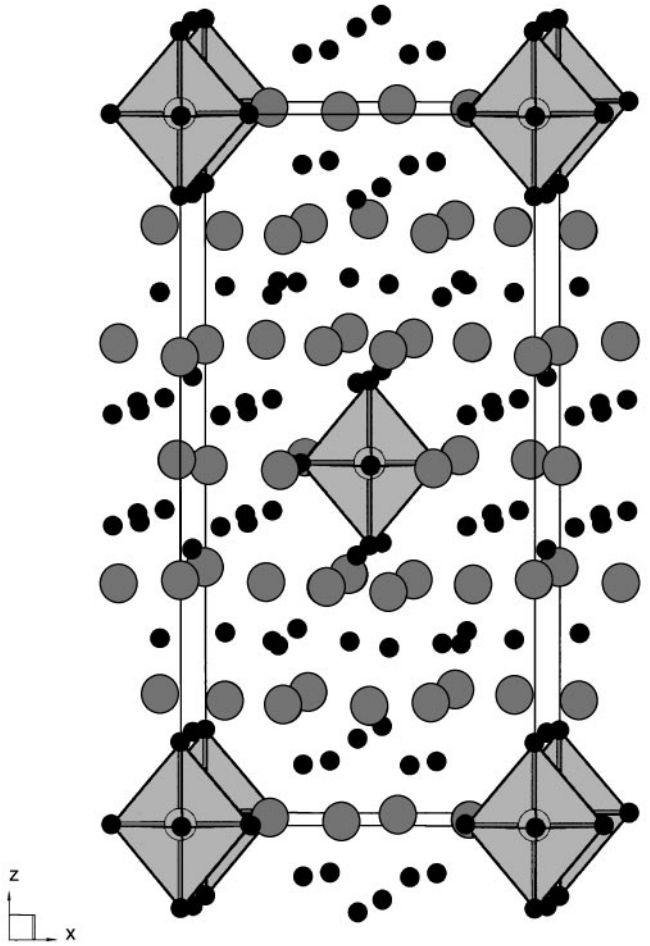

FIG. 5. The Rietveld-refined (neutron plus X-ray) structure of Type Ia $Bi_{14}WO_{24}$ (20). Bismuth atoms are darker than tungsten atoms and oxygen atoms are black. Average, disordered, WO_6 octahedra are shown.

group symmetry to be $I4_1$ but pseudo-$I4_1/a$. There was no evidence to indicate that the unit cell or space-group symmetry were functions of composition, requiring the presence of some compositional disorder in the structure of the phase to account for the solid-solution range.

Watanabe *et al.* (26) used precession photography of a single-crystal to determine the space group of $Bi_{14}W_2O_{27}$ (at the bismuth-rich end of the solid-solution) to be $I4_1/a$. A model was proposed in that space group in which W atoms were located on 4*a* and 4*b* sites (the former being fully occupied by W atoms and the latter being a mixed-metal site). These sites are isolated from one another such that there can be no W–O–W bonds; i.e., the *M* atoms are isolated in a similar fashion to those in Type I $Bi_{15}TaO_{25}$ and Type Ia $Bi_{14}(W/Mo)O_{24}$. The distribution of oxygen atoms was modeled as a partially occupied fluorite-type array. Zhou *et al.* (15) tested this model using image matching/multislice techniques with ED and HRTEM data, and found it to be plausible.

Single-crystals with a range of compositions within the solid-solution field (including $Bi_{14}W_2O_{27}$) were recently grown (19) and examined on a single-crystal X-ray diffractometer using Mo$K\alpha_1$ radiation ($\lambda = 0.7107$ Å) from a rotating-anode source. The intensity of the satellite reflections was extremely low, as expected from XRD data (see Fig. 12 of Ling *et al.* (18)). It was only possible to adequately assess the quality of large crystals (edge dimensions ~ 50–$100\,\mu m$) for which a reasonable number of satellite reflections were observable. These crystals, which were too large for data collection due to the massive absorption coefficient of the compound, suffered badly from twinning of the tetragonal (but pseudo-cubic) subcell. Furthermore, the profiles of reflections, even in untwinned crystals, indicated that the composition (hence the cell dimensions) was slightly inhomogeneous, resulting in "smeared" reflections.

Synchrotron XRD and neutron powder diffraction data were used (19) to test, extend, and partially refine the model of Watanabe *et al.* (Note that Watanabe *et al.* used origin choice no. 2 for $I4_1/a$; in this study, origin choice no. 1 is used; i.e., the coordinates are shifted by $(0\,\frac{1}{4}\,\frac{1}{8})$.) Data from two compositions within the solid-solution were used, $Bi_{14}W_2O_{27}$ (12.5 mol% W_2O_6) and $Bi_{22}W_4O_{45}$ (15.4 mol% W_2O_6).

The final model is shown in Fig. 6 and listed in Table 1. Metal atom positions were Rietveld-refined in $I4_1/a$ using synchrotron XRD data, which have very little sensitivity to oxygen atoms due to the presence of strongly scattering Bi and W atoms. Refinement of independent isotropic displacement parameters, and of fractional occupancies in conjunction with an overall isotropic displacement parameter, strongly supported the metal atom compositional ordering scheme of Watanabe *et al.* The model therefore involves a mixed metal atom site (M1), the composition of which is 25% W for $Bi_{14}W_2O_{27}$ and 54% W for $Bi_{22}W_4O_{45}$. Lowering the space-group symmetry to $I4_1$ failed to give reliable results due to under-determination of the additional variables by powder data, which contained extensive reflection overlap.

Attempts to Rietveld-refine fluorite-type oxygen atom positions using neutron powder diffraction data also failed due to extensive reflection overlap. The careful and systematic use of Fourier synthesis techniques did, however, lead to the identification of one unoccupied fluorite-type oxygen atom site. This site coordinated W1 twice; i.e., its absence reduced the coordination number of W1 from 8-fold to 6-fold, a much more chemically plausible environment. This also improved the stoichiometry, which in the case of $Bi_{22}W_4O_{45}$ required 8.65/10 fluorite-type oxygen atom vacancies.

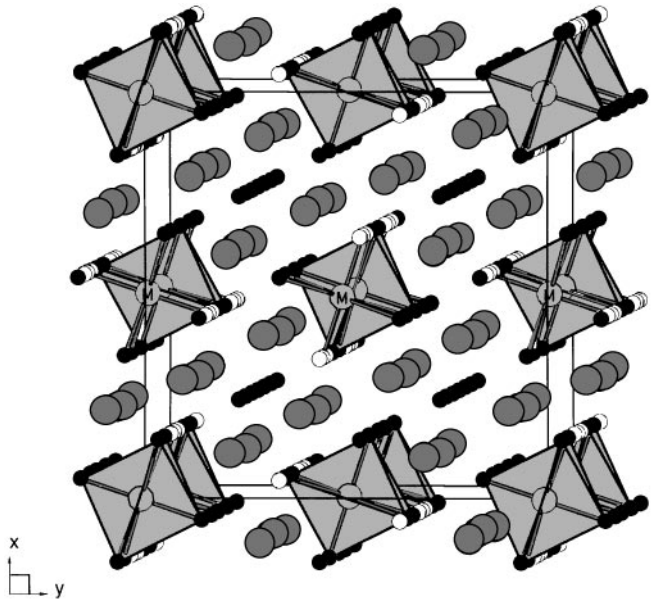

FIG. 6. The disordered, partly Rietveld-refined (neutron plus X-ray) structure of the Bi_2O_3–WO_3 Type Ib solid-solution (19). Bismuth atoms are darker than tungsten atoms, oxygen atoms are black, and partially occupied oxygen atom sites are white. Mixed occupancy metal atom sites are labeled "*M*". WO_6 octahedra and *M*–O bonds are shown.

After the remaining required oxygen vacancies on one of the fluorite-type oxygen sites which doubly coordinates the mixed metal site (54% W in $Bi_{22}W_4O_{45}$) was located, a model was proposed in which the percentage of tungsten on the mixed metal site corresponds to the percentage of oxygen missing from the adjacent fluorite-type oxygen site. Positions O2 and O10 are both averaged from two fluorite-type oxygen atom positions in order to create more regular octahedra. In the case of $Bi_{22}W_4O_{45}$, 35% oxygen vacancy does not match 54% W; however, the two values do match (at 42.85%) for the composition Bi_6WO_{12}, which falls between $Bi_{14}W_2O_{27}$ and $Bi_{22}W_4O_{45}$, i.e., within the solid-solution range observed in previous studies (15, 18, 26). A similar argument was used by Zhou *et al.* (15) to propose a tungsten-rich upper limit on the Type Ib composition of Bi_6WO_{12}.

This type of model can exist in $I4_1$ but not in $I4_1/a$, because the *a*-glide links fluorite-type oxygen sites around the tungsten and mixed metal sites such that ordered 6-fold coordination cannot be achieved in $I4_1/a$. Given the observed weak breaking of the *a*-glide (18), it therefore seems likely that this pattern of oxygen vacancies is the driving force behind symmetry lowering. The relative orientations of the octahedra shown in Fig. 6 were determined by the systematic comparison of all possibilities against neutron powder diffraction data (19), although it should be noted that the best results (obtained for the model in Table 1) were only marginally better than some other possible models and therefore are by no means definitive.

This model is very much an average solution. It reflects the compositional disorder suggested at the outset by the lack of any apparent correlation among solid-solution composition, unit cell dimensions, and space-group symmetry. It is likely that the true structure is of a lower space-group symmetry, disordered through repeated twinning. Importantly, while a sophisticated model such as this could conceivably remove the necessity for a mixed-metal site at certain compositions, it could not remove the necessity for a slight oxygen deficiency at compositions more tungsten-rich than Bi_6WO_{12}. Although Zhou *et al.* (15) reported Bi_6WO_{12} as the upper limit of the solid solution field, slightly more tungsten-rich compositions have been found by Ling *et al.* (18) and Watanabe *et al.* (26). This problem might be explained by the partial reduction of W^{6+} to W^{5+}; the model shown in Fig. 6 would then actually be approximately $Bi_{22}W^{6+}_2W^{5+}_2O_{44}$ rather than $Bi_{22}W^{6+}_4O_{45}$. This is a quite plausible explanation given that W^{6+} is easily reduced at high temperatures, as indicated by the series WO_{3-x} ($0 \le x \le 3$) (27). It must be noted, however, that no darkening in color was observed as expected for reduced tungsten oxides, suggesting that the extent to which any such reduction occurs must be quite limited.

TABLE 1

The Disordered, Partly Rietveld-Refined Structure of the Bi_2O_3–WO_3 Type Ib Solid-Solution at the Composition $Bi_{22}W_4O_{45}$ (Space group $I4_1$ (no. 80), $a = 12.49687(8)$, $c = 11.24558(14)$ Å)

	x (*a*)	*y* (*b*)	*z* (*c*)	Fraction[a]	$100U_{iso}$ (Å^2)
Bi1	0.2959(2)	0.6064(2)	0.10110(12)	1	2.43(8)[b]
Bi2	0.2117(2)	0.8967(2)	0.1309(2)	1	2.43(8)[b]
Bi3	0.7041(2)	0.8936(2)	0.89890(12)	1	2.43(8)[b]
Bi4	0.7883(2)	0.6033(2)	0.8691(2)	1	2.43(8)[b]
W1	0	0.5	0.125	1	2.43(8)[b]
M1	0	0.5	0.625	0.46 W 0.54 Bi	2.43(8)[b]
O1	0.05	0.85	0.25	1	13.8(2)[b]
O2	0.15	0.55	0.125	1	13.8(2)[b]
O3	0.25	0.75	0.25	1	13.8(2)[b]
O4	0.35	0.95	0.25	1	13.8(2)[b]
O5	0.55	0.85	0.75	1	13.8(2)[b]
O6	0.65	0.55	0.75	0.46	13.8(2)[b]
O7	0.75	0.75	0.75	1	13.8(2)[b]
O8	0.85	0.95	0.75	1	13.8(2)[b]
O9	0.95	0.65	0.75	0.46	13.8(2)[b]
O10	0.95	0.65	0.825	0.54	13.8(2)[b]

[a] Determined from stoichiometry (oxide ratio during synthesis), not refined.

[b] Constrained to be equal.

Bi_2O_2–Nb_2O_5 and Bi_2O_3–Ta_2O_5 Type II

Structural models at various compositions within these solid-solution ranges (6.25–23.4 mol% Nb_2O_5 and 10–25 mol% Ta_2O_5 (23, 39)) were proposed by Zhou *et al.* (7, 14, 16), by incorporating tetrahedral clusters of (Nb/Ta)O_6 octahedra (a motif found in pyrochlore-type (Fig. 3*c*)) into the δ-Bi_2O_3-related matrix to create fluorite-type superstructures. Withers *et al.* (23) recently redescribed Type II in terms of superspace group symmetry as a three-dimensional incommensurately modulated phase (18), and they used that description to parameterize the associated compositional and displacing degrees of freedom (23). The atomic modulation functions describing metal and oxygen atom distributions within the fluorite-type subcell array were both found to be closely related to a three-dimensional shape known as the "D" Periodic Nodal Surface. The small number of satellite reflections observed in synchrotron XRD and neutron powder diffraction at several compositions allowed limited testing of possible models within this framework.

Part of a representative model for this phase, at the composition $Bi_8(Nb/Ta)_2O_{17}$, which provided a reasonable match to observed data, is shown in Fig. 7. This model corresponds to $\varepsilon = \frac{3}{8}$, $\delta_1 = \delta_2 = \delta_3 = \frac{3}{16}$, and $\varphi_O(1\,1\,1) = 90^\circ$, i.e., Figs. 4b and 7a in Withers *et al.* (23). This model is significantly different from those described above, in that *M* atoms are no longer isolated from one another within a fluorite-type subcell framework. In terms of the relationship of this model to pyrochlore-type (Fig. 3a), both

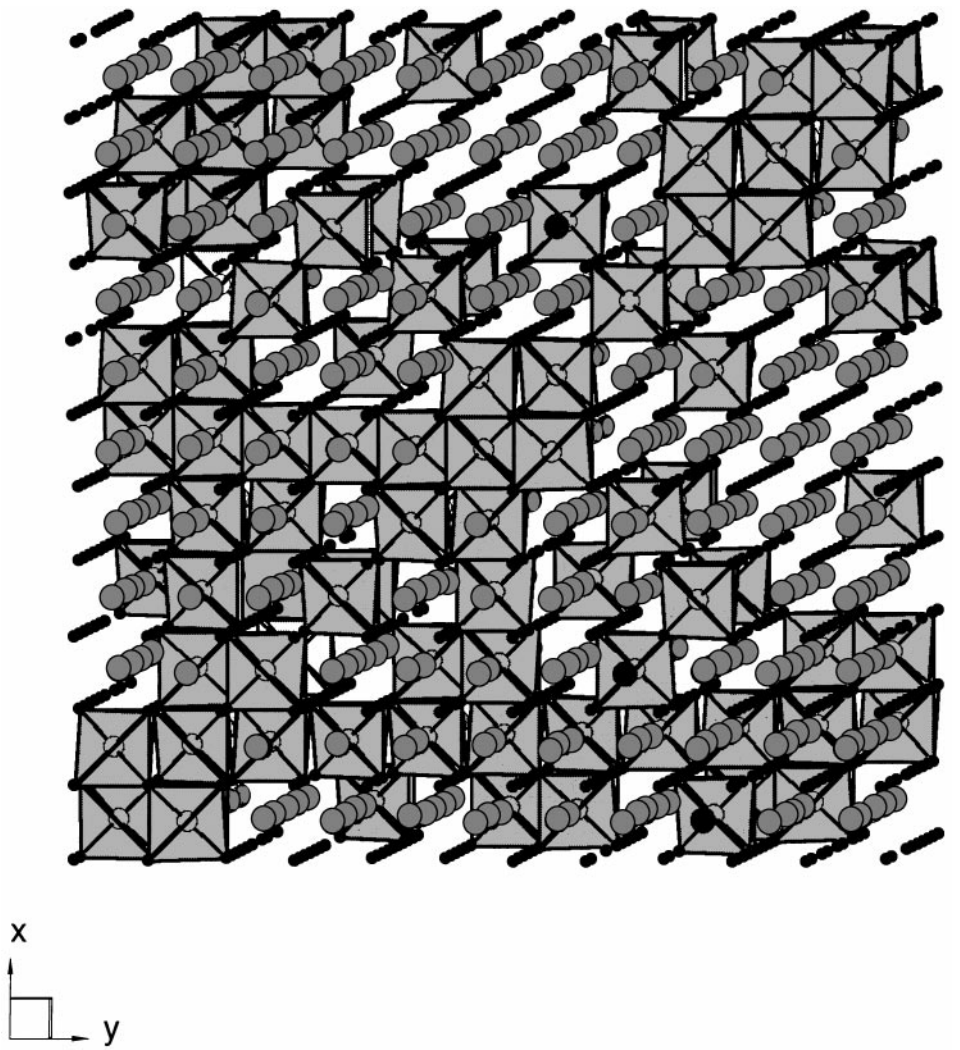

FIG. 7. The (unrefined) metal atom plus oxygen atom vacancy ordering model for the Bi_2O_3–$(Nb/Ta)_2O_5$ Type II solid-solution at the composition $Bi_8(Nb/Ta)_2O_{17}$, using $\varepsilon = 3/8$, $\delta_1 = \delta_2 = \delta_3 = 3/16$, $\varphi_O(1\,1\,1) = 90^\circ$ (23). The model shown incorporates $5 \times 5 \times 5$ fluorite-type subcells. Bismuth atoms are darker than niobium/tantalum atoms, and oxygen atoms are black. (Nb/Ta)O_6 octahedra are shown.

the cluster (Fig. 3c) and the string (Fig. 3d) motifs are evident. At more bismuth-rich compositions, isolated $(Nb/Ta)O_6$ octahedra (Fig. 3b) are also observed in this type of model. Nonetheless, while there is no strict adherence to any one motif, the string motif does appear to be dominant.

The structure of the Bi_2O_3–$(Nb/Ta)_2O_5$ Type II phase can be most usefully interpreted as strings of Nb/Ta atoms within a fluorite-type metal atom array, arranged along three of the six possible $\langle 1\,1\,0\rangle_F$ directions, e.g., $[1\,1\,0]_F$, $[1\,0\,1]_F$, and $[0\,1\,1]_F$; i.e., no two of the string directions are coplanar perpendicular to a particular $\langle 1\,0\,0\rangle_F$ direction and all the strings are at 60° to one other. Incommensurate variability in both the spacing and the continuity of these strings permits the wide compositional solid solution.

Bi_2O_3–MoO_3 38:7

The line phase $Bi_{38}Mo_7O_{78}$ reported by Buttrey *et al.* (7) was reproduced in a recent study (18) at the same composition. ED analysis was in agreement with the conclusion of Buttrey *et al.* that the phase was a $3a_F$, $5b_F$, $3c_F$ superstructure of fluorite-type and that the space-group symmetry was unambiguously orthorhombic *Pccn*.

Buttrey *et al.* noted that for a $3 \times 5 \times 3$ fluorite-type metal atom array in *Pccn*, all metal atoms are on general positions with a multiplicity of 8, with the exception of the inversion center (multiplicity = 4). In order to comply with the stoichiometry $Bi_{38}Mo_7O_{78}$, $z = 4$, this special position must be occupied by an Mo atom. A complete model of the metal atom array then requires a further three (general position) metal atom sites to be occupied by Mo atoms. They noted further that the presence of a molybdenum atom on an inversion center implied octahedral, rather than tetrahedral, coordination of Mo atoms by oxygen atoms. They speculated that the arrangement of the three additional Mo atom sites about the inversion center would resemble a unit of pyrochlore-type, allowing oxygen vacancies to be accommodated, but they did not elaborate on this arrangement.

Single-phase powder samples of $Bi_{38}Mo_7O_{78}$ grown at stoichiometry recently (19) were highly crystalline and contained large numbers of crystals suitable for single-crystal synchrotron X-ray diffraction. It was hoped that single-crystal data could be collected and used to elucidate the structure of the phase. A large number of crystals were investigated at the Photon Factory (KEK, Tsukuba, Japan), the majority of which displayed good cell dimensions, peak shapes, and satellite reflection intensities. In all cases, however, it was found that $\beta = 90.6°$ despite evidence from synchrotron XRD (18) that the cell was orthorhombic. This observed monoclinic splitting originates in the pseudo-tetragonal nature of the unit cell, where $a \sim c$ (see Table 2 of Ling *et al.* (18)), resulting in endemically twinned crystals in which mismatches occur between *a* and *c*. It can easily be shown trigonometrically that this leads to the observed 90.6° angle between a^* and c^*. It was not considered worthwhile collecting synchrotron X-ray data from such crystals, and it proved impossible to prepare true single crystals of this phase. An attempt was therefore made recently (19) to determine the structure of $Bi_{38}Mo_7O_{78}$ using only synchrotron XRD and powder neutron diffraction data.

Two models were initially proposed for $Bi_{38}Mo_7O_{38}$, based, respectively, on tetrahedral clusters of MoO_6 octahedra (Fig. 3*c*) and on continuous $\langle 1\,1\,0\rangle_F$ strings of MoO_6 octahedra (Fig. 3d). Building solely from the first of these motifs allows only one possible model for the structure of $Bi_{38}Mo_7O_{78}$, given the restrictions of space group, unit cell, and stoichiometry. This model is shown in Fig. 8a. This cluster model has stoichiometry $Bi_{38}Mo_7O_{82}$; i.e., only a small number of additional oxygen atom vacancies are required in the bismuth-rich regions of the structure to fully comply with stoichiometric requirements.

Despite the appealing way in which the cluster motif can be used to build an unambiguous structural model for $Bi_{38}Mo_7O_{78}$, the model itself did not satisfactorily fit observed XRD or neutron powder diffraction data (19). The model was also at odds with HRTEM images published by Buttrey *et al.* (7). These images clearly show a stepped, diamond-like contrast pattern in the $[1\,0\,1] = [1\,0\,1]_F$ projection, but no such distinct contrast pattern in the $[0\,3\,5] = [0\,1\,1]_F$ projection. The cluster model fails to explain either the diamond-like pattern or the reason behind any significant difference between the contrast patterns in different $\langle 1\,1\,0\rangle_F$ projections.

The alternative model, constructed using the string motif from pyrochlore-type, requires the construction of the longest possible strings of MoO_6 octahedra along $\langle 1\,1\,0\rangle_F$ directions. Because of the $3 \times 5 \times 3$ fluorite-type superstructure, infinite strings are only possible perpendicular to the long (*b*) axis. Given the space-group symmetry and the presence of an Mo atom on the inversion center, this would place all Mo atoms in parallel "cross" patterns at $z = 0$ and $z = 1/2$. Such a "cross" pattern cannot, however, provide the correct stoichiometry, placing 20 Mo atoms in the unit cell where 28 are required. Such a model also conspicuously fails to account for the HRTEM observations of Buttrey *et al.* A diamond-like contrast pattern would be generated in the $[0\,3\,5] = [0\,1\,1]_F$ and $[5\,3\,0] = [1\,1\,0]_F$ projections but not in the $[1\,0\,1] = [1\,0\,1]_F$ projection where a layered contrast pattern would be generated. Furthermore, the diamond-like pattern would not be "stepped" as observed.

In order for a string model to fit the observed HRTEM contrast pattern, it is necessary to orient the strings perpendicular to the *c* axis of the supercell. Unfortunately, the 5×3 fluorite-type cross section in this direction rules out the

possibility of infinite strings of MoO_6 octahedra. The arrangement which gives the longest continuous strings and the desired stoichiometric ratio is shown in Fig. 8b. This model generates a stepped, diamond-like contrast pattern in the [1 0 1] projection and no contrast pattern in the [0 3 5] or [5 3 0] projections, as observed in HRTEM (7). XRD and powder neutron diffraction data also qualitatively support the string model over the cluster model (19), although in neither case was it possible to actually refine the models using powder data. Note that the "steps" in the $\langle 1\,1\,0\rangle_F$ strings form triangles of three Mo atoms on $\langle 1\,1\,1\rangle_F$ planes; i.e., the faces of tetrahedra from the cluster motif (Fig. 3c).

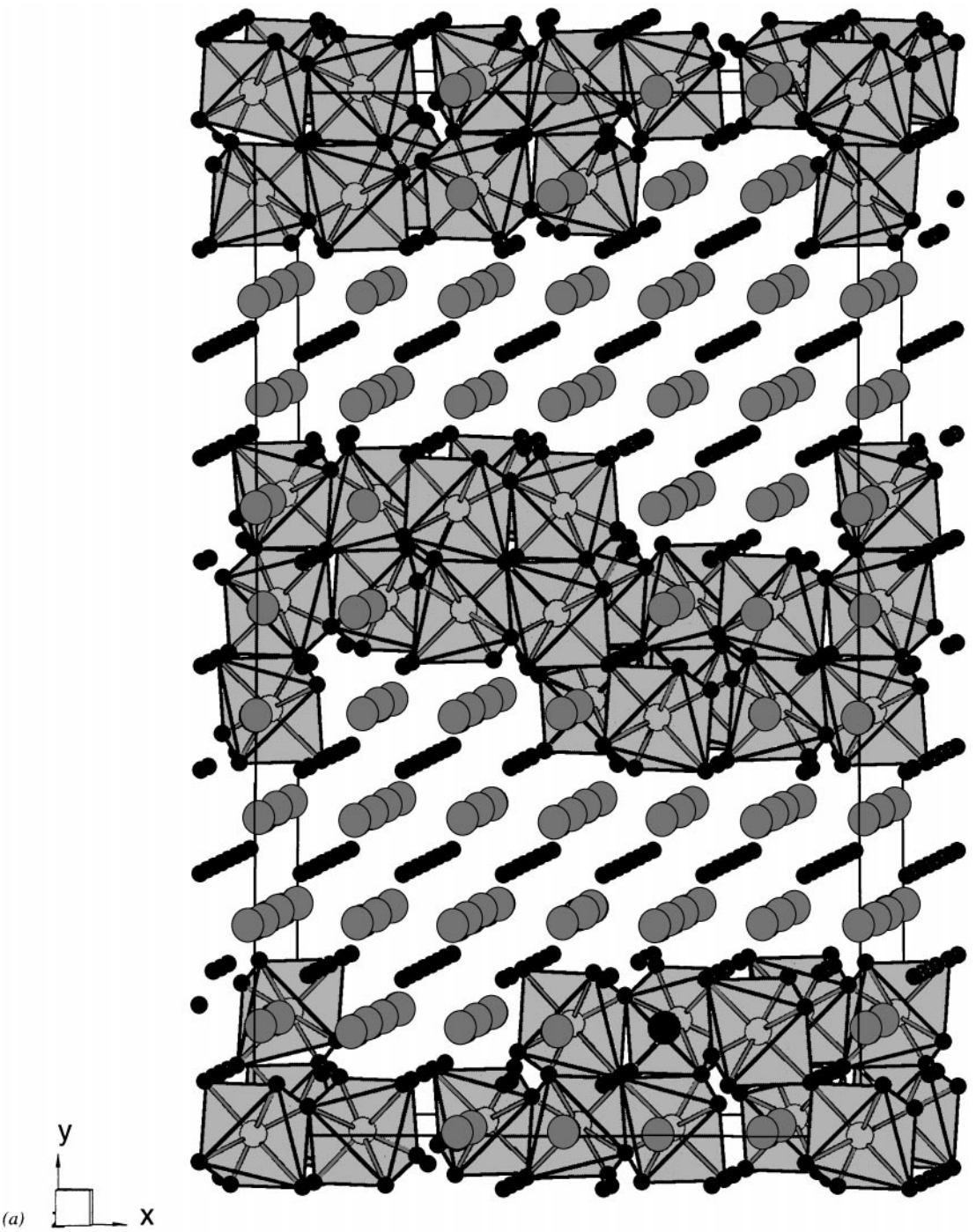

FIG. 8. The (unrefined) metal atom plus oxygen atom vacancy ordering models for $Bi_{38}Mo_7O_{78}$ (19), based on the (a) cluster and (b) string motifs from pyrochlore-type. Bismuth atoms are darker than molybdenum atoms and oxygen atoms are black. MoO_6 octahedra are shown.

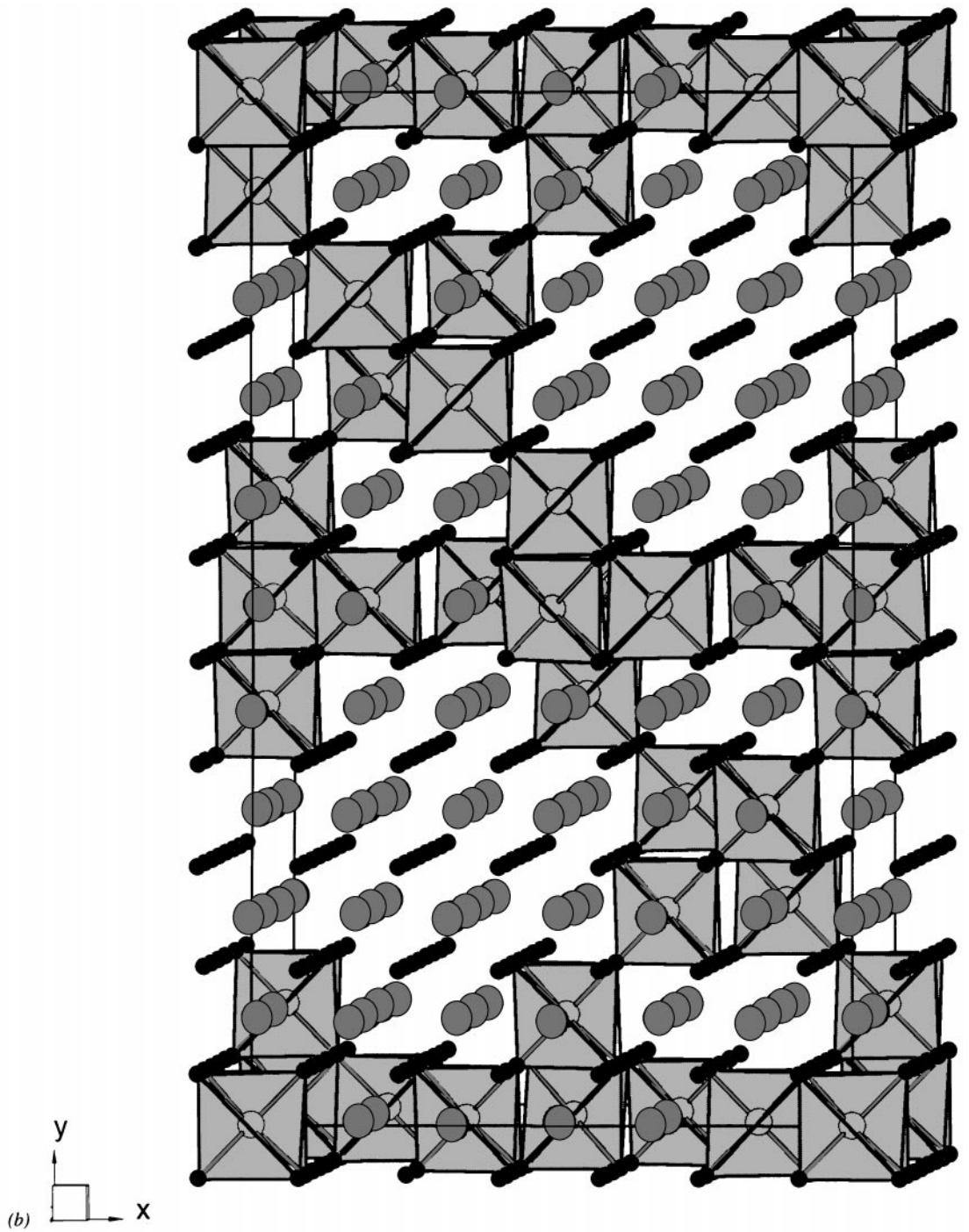

FIGURE 8—*Continued*

The overall stoichiometry is $Bi_{38}Mo_7O_{83}$; i.e., again, a small number of additional oxygen vacancies are required in the bismuth-rich regions of the model.

As for the Bi_2O_3–$(Nb/Ta)_2O_5$ Type II solid-solution phase described above (Fig. 7), the dominant structural motif in this structure (Fig. 8b) is continuous $\langle 1\,1\,0\rangle_F$ strings (albeit occasionally stepped along the $[1\,0\,1]_F$ and $[1\,0\,\bar{1}]_F$ directions) of MO_6 octahedra. Unlike the Type II phase, however, strings are arranged along only two of the six possible $\langle 1\,1\,0\rangle_F$ directions, $[1\,1\,0]_F$ and $[1\,\bar{1}\,0]_F$; i.e., both string directions are perpendicular to $[0\,0\,1]_F$. Note that strings in alternate $\langle 1\,1\,0\rangle_F$ directions are never actually

coplanar perpendicular to $[0\,0\,1]_F$. It is the nature of the interactions between the strings that differentiates the structure types. Clearly, $\langle 1\,1\,0\rangle_F$ strings of MO_6 octahedra represent a very versatile structural motif by which pyrochlore-type units may be incorporated into fluorite-type.

Bi_2O_3–Nb_2O_5 Type III

This phase is a superstructure of fluorite-type δ-Bi_2O_3 (9, 18). The possibility therefore exists of determining the structure absolutely given sufficient data. Two previous attempts have been made, using different data types and methodologies. Zhou *et al.* (9) used image matching/multislice methods with HRTEM and ED data to propose a model based on the pyrochlore-type cluster motif (Fig. 3c). The interaction of the clusters with one another in this model creates some perovskite-type regions, such that the model appears to be a composite of fluorite, pyrochlore, and perovskite types. This appeared reasonable given that the parent structure was clearly fluorite-type, that the slightly more bismuth-rich Type II phase was thought to contain such clusters (15, 18), and that the slightly more bismuth-poor Type IV phase was thought to contain perovskite-type units (19, 20). However, in light of the recent reinterpretation of the relationship of the Type II structure to pyrochlore-type (23), it was clearly necessary to re-examine this Type III model.

More recently, the structure of Bi_3NbO_7 was the subject of a single-crystal X-ray diffraction study by Castro *et al.* (28). The satellite reflections clearly visible in ED and XRD (9, 18) were not observed in the single crystal, and the study made use only of the subcell reflections. The structure was refined in $Fm\bar{3}m$, i.e., as fluorite-type, with mixed occupancy on the metal atom site. Only one positional parameter is refined, the x-coordinate of the oxygen site, which was shifted from $x = 1/4$ to $x = 0.189(9)$ (i.e., ~ 0.3 Å shift) in order to introduce some disorder, after the δ-Bi_2O_3 model refined by Battle *et al.* (5). It is important to note that Castro *et al.* analyzed their material by ED and HRTEM and found it to be of Type II. The fact that Castro *et al.* analyzed their material and confirmed the composition as 25 mol% Nb_2O_5 therefore suggests that the Type II solid-solution range may actually extend to 25 mol% Nb_2O_5. This is consistent with the observation by Ling *et al.* (18) using EDXA analysis of a two-phase region containing regions of 23.4(4) mol% Nb_2O_5 (Type II) and 25.5(2) mol% Nb_2O_5 (Type III); i.e., the exact stoichiometry of Type III is slightly more Nb_2O_5–rich than Bi_3NbO_7. Given that their crystal was of Type II, for which extremely weak satellite reflections have been observed in synchrotron XRD data (18, 23), the failure of Castro *et al.* to observe any weak satellite reflections in XRD or single-crystal X-ray diffraction can perhaps be attributed to the use of less intense conventional X-ray sources.

Crystals grown by the present author using the slow-cooling method of Castro *et al.* and examined on a single-crystal diffractometer were found to have poor peak shapes and cubic (rather that tetragonal) subcells. Satellite reflections corresponding to the Type III superstructure were observed; however, they were far weaker than expected on the basis of XRD data. It appears that macroscopic crystals do not fully order due, presumably, to repeated twinning of the tetragonal, but pseudo-cubic, subcell. The poor peak shapes and cubic subcell may have been due to overlapping twin reflections, and the poor satellite intensities to their dilution by three-way twinning. Attempts to grow crystals by slow-cooling of two-phase mixtures with either Type II or IV (see the phase diagram in Fig. 2 of Ling *et al.* (18)) failed to produce crystals of higher quality.

In the absence of useful single crystals, neutron powder diffraction and synchrotron XRD data were recently used in an attempt to determine the structure of this phase (19). It has been shown (18) that there is a probable relationship between the primary modulation wave-vector of the Type II Bi_2O_3–Nb_2O_5 phase and that of Type III Bi_3NbO_7. The first stage in arriving at a structural model for Bi_3NbO_7 was therefore to consider the adjacent Type II structure.

The unit cell of Bi_3NbO_7 can be described as an F-centered $3 \times 3 \times 7$ supercell of fluorite-type, or alternatively as a $\frac{3}{2}(\mathbf{a}_F + \mathbf{b}_F)$, $\frac{3}{2}(-\mathbf{a}_F + \mathbf{b}_F)$, $7\mathbf{c}_F$ I-centered supercell. Either description is incompatible with a commensurate version of the Type II phase, which ought to be cubic. Previous HRTEM work (9), however, indicates the way in which this incompatibility might be resolved; the structure is clearly "layered," with a repeat of 3.5 fluorite-type unit cells. The observed image contrast implies the presence of a bismuth-rich layer in the metal atom array twice per unit cell perpendicular to the long (c) axis. The remaining metal atoms in the unit cell therefore comprise two $3 \times 3 \times 3$ fluorite-type blocks, symmetrically related by the observed F-centering of the $3 \times 3 \times 7$ Type III supercell.

Modeling of the structure of Bi_3NbO_7 began by treating this $3 \times 3 \times 3$ fluorite-type block analogously to the Type II phase described above. In terms of the equations of Withers *et al.* (23), this corresponds to the choice $\varepsilon = \frac{1}{3}$. The superspace group symmetry of the Type II phase $P{:}Fm\bar{3}m{:}Fd\bar{3}m$ can then be reduced to a conventional space group symmetry for certain choices of δ_1, δ_2, and δ_3. The highest possible resultant $3 \times 3 \times 3$ space group symmetry consistent with a tetragonal $3 \times 3 \times 7$ supercell is $F\bar{4}3m$, obtained when $\delta_1 = \delta_2 = -\frac{1}{8}$, $\delta_3 = \frac{3}{8}$. The $\bar{4}3m$ point group symmetry of this space group is essentially that of a tetrahedron.

Incorporating two such $F\bar{4}3m$ blocks into the $3 \times 3 \times 7$ supercell, and taking into consideration the observed centering, the resultant space group symmetry reduces to $F\bar{4}2m$ with respect to the $3 \times 3 \times 7$ supercell, or $I\bar{4}m2$ (no. 119) with respect to the $\frac{3}{2}(\mathbf{a}_F + \mathbf{b}_F)$, $\frac{3}{2}(-\mathbf{a}_F + \mathbf{b}_F)$, $7\mathbf{c}_F$ I-centered supercell. This symmetry lowering can be thought

of in terms of "stretching" a tetrahedron along its $\bar{4}$ axis; its $\bar{4}$ axis, 2-fold axis, and mirror plane are preserved but its 3-fold axis is broken. The space group $I\bar{4}m2$ is compatible with selected area ED observations (Fig. 5 of Ling *et al.* (18)), which suggested a maximum symmetry space group $I4/mmm$ (adding an inversion center to a point group symmetry of $\bar{4}m2$ implies Laue symmetry of $4/mmm$). The space group symmetry is lowered by breaking the mirror plane perpendicular to c, a symmetry element that was not compatible with the $3 \times 3 \times 3$ block concept. The presence or otherwise of an inversion center is difficult to detect by selected area ED.

This I-centered ($\frac{3}{2}(\mathbf{a}_F - \mathbf{b}_F)$, $\frac{3}{2}(\mathbf{a}_F + \mathbf{b}_F)$, $7\mathbf{c}_f$) cell contains $(3 \times 3 \times 7) \times 2 = 126$ metal atom sites, of which 32 (25.4%) should be Nb to most closely match the composition determined (18) from starting materials in synthesis, as 25% and by EDXA as 25.5(2) %. The proposed model calls for two of the 14 metal atom layers perpendicular to the long axis c, at $z = 0$ and $z = 1/2$, to be pure Bi. The $3 \times 3 \times 3$ fluorite-type blocks should therefore each contain 32 Nb atoms, i.e., 29.63%.

Fourier difference techniques were used (19) with low-angle (5–45°2θ) synchrotron XRD data in order to find a metal atom compositional ordering pattern that satisfied both the low-angle XRD data and the required composition. One solution above all others investigated was found to give a remarkably good fit to the low-angle satellite reflections, ignoring any displacing modulation away from the fluorite-type subcell positions. Fluorite-type oxygen atom vacancies were introduced, after the manner shown in Fig. 2, and fluorite-type oxygen atom positions were distorted after the manner shown in Fig. 3. The model is shown in Fig. 9 (note that the standard $I\bar{4}m2$ setting is used) and the coordinates are listed in Table 2. Attempts to refine metal atom positions using synchrotron XRD data, and oxygen atom positions using neutron powder diffraction data, failed due to the extensive peak overlap in this powder data. A full refinement will require single-crystal X-ray diffraction data, if and when it is possible to grow a useful single-crystal for the collection of these data.

This model can be partly, but not entirely, described in terms of the tetrahedral cluster motif from pyrochlore-type (Fig. 3*c*). On consideration, however, it is not in fact possible to construct a model of the required composition in this space group based solely on the tetrahedral motif while retaining the two pure bismuth layers implied by HRTEM. If all eight nontetrahedral Nb atoms were removed, two Nb_4 tetrahedra would be required to restore the correct stoichiometry. These could only be incorporated by destroying the integrity of the pure Bi layers; therefore more complex units of corner-connected tetrahedra must be invoked. The $3\mathbf{a}_F$, $3\mathbf{b}_F$ fluorite-type basal plane of the supercell does not, however, permit continuous strings of corner-connected Nb_4 tetrahedra to be constructed, and therefore the symmetry would have to be lowered to allow any units more complex than isolated tetrahedra. In particular, the $\bar{4}$ element would be destroyed, reducing the cell symmetry from tetragonal to orthorhombic. Given that no orthorhombic distortion is observed, even in high-angle synchrotron XRD data, it is very hard to justify this lowering of symmetry. The model proposed here, therefore, incorporates the Nb_4 tetrahedral motif from pyrochlore-type as far as is possible in a tetragonal space group.

The model can also be partly, but not entirely, described in terms of the $\langle 1\,1\,0 \rangle_F$ string motif from pyrochlore-type (Fig. 3d). Again, however, on consideration it becomes apparent that complete adoption of this motif is precluded by the nature of the unit cell. Continuous strings cannot be accommodated in the four $\langle 1\,1\,0 \rangle_F$ directions which have a component along c without some disjunction. Even with the presence of such a disjunction (on the pure Bi layers), it would still be necessary to break tetragonal symmetry in the I-centered cell to accommodate these strings. Furthermore, in the proposed metal atom ordering model, the isolated Nb_4 tetrahedra can be interpreted as continuous strings identical to those containing the other Nb atoms but with only $\frac{2}{3}$ occupancy (Bi6 being a Bi site rather than an Nb site), an unavoidable consequence of the composition. In this sense, the proposed model incorporates $\langle 1\,1\,0 \rangle_F$ Nb strings as far as is possible in a tetragonal space group.

Given that the structure of Bi_3NbO_7 is a $\frac{3}{2}(\mathbf{a}_F - \mathbf{b}_F)$, $\frac{3}{2}(\mathbf{a}_F + \mathbf{b}_F)$, $7\mathbf{c}_F$ superstructure of fluorite-type, that the cell is tetragonal, and that it contains two pure Bi layers perpendicular to c, the proposed model is clearly more probable than any alternative. It has the most probable symmetry, it incorporates Nb atoms in the most chemically sensible way (according to the ordering scheme of the archetypal pyrochlore-type), and it fits low-angle XRD data remarkably well without the introduction of any displacing modulations from a fluorite-type parent.

Although Zhou *et al.* (9) give no coordinates, space group, or even crystal system for their metal atom ordering model, it is clear from the (incomplete) picture published that its symmetry is lower than tetragonal, possibly even lower than orthorhombic. As discussed above, there is simply no evidence for this symmetry lowering. The picture published by Zhou *et al.* is actually very hard to interpret. It appears to show eight of the 14 metal atom layers perpendicular to c as a continuous network of corner-connected NbO_6 octahedra on $[1\,1\,1]_F$ planes, an impossible arrangement given that the $3 \times 3 \times 7$ fluorite-type supercell they use is quite clearly F-centered. The disordered model of Castro *et al.* (28) apparently refers to the subcell of the Type II phase and therefore cannot be compared with the model proposed in the present study.

Despite the strong reciprocal space relationship between the Type II and III phases in the Bi_2O_3–Nb_2O_5 systems, there are some clear differences between these real space

structures as shown in Figs. 7 and 9. The most important difference is that not only has the number of independent $\langle 1\,1\,0\rangle_F$ directions in which continuous Nb strings are observed reduced from three to two but also the relative orientations of these directions are different. In Type II, each of the three $\langle 1\,1\,0\rangle_F$ strings is perpendicular to a different $\langle 1\,0\,0\rangle_F$ direction, whereas in Type III, both strings are perpendicular to the same $\langle 1\,0\,0\rangle_F$ direction. Re-examining

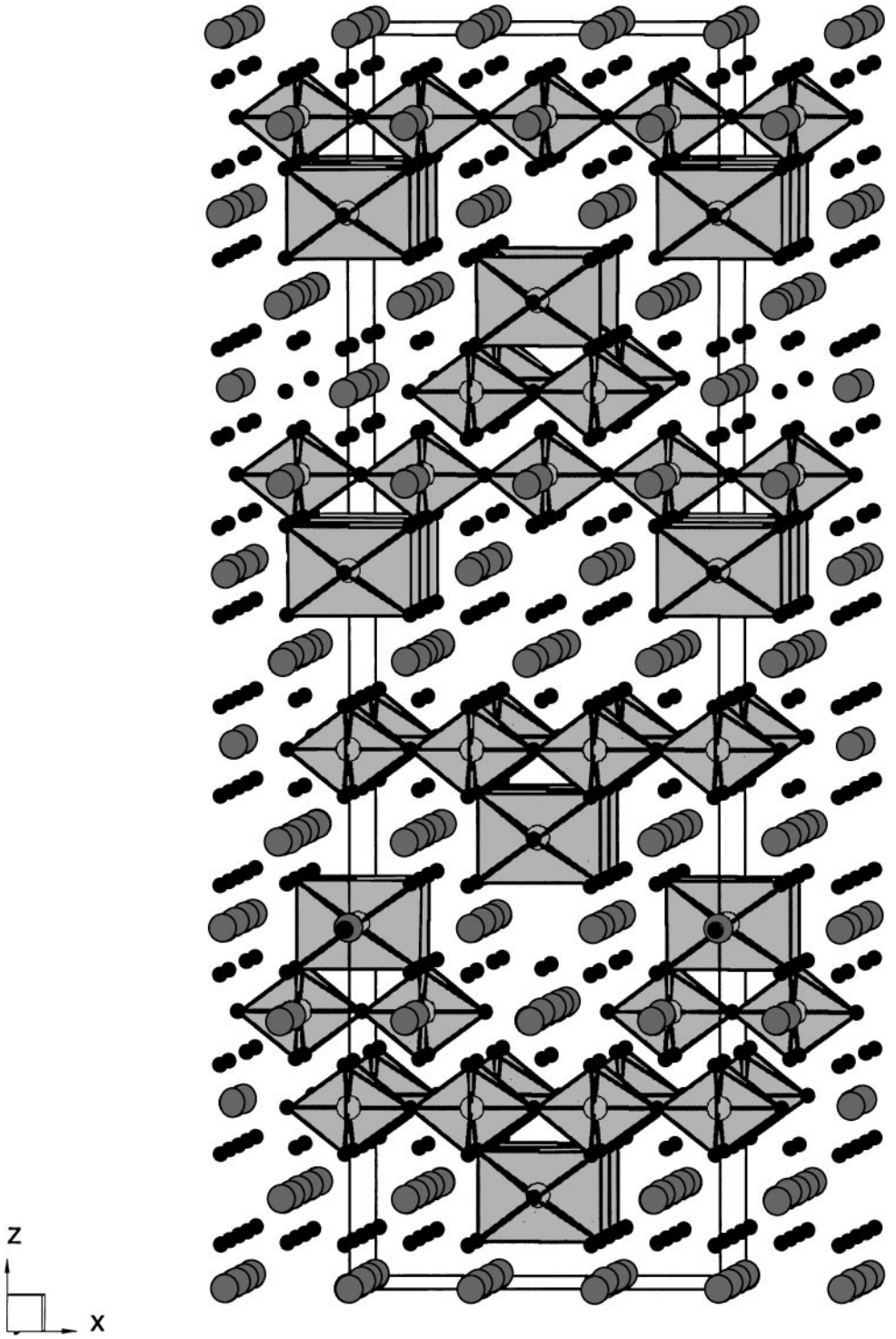

FIG. 9. The (unrefined) metal atom plus oxygen atom vacancy ordering model for Type III Bi_3NbO_7 (19). Bismuth atoms are darker than niobium atoms and oxygen atoms are black. NbO_6 octahedra are shown.

TABLE 2
Factional Atomic Coordinates and Equivalent Isotropic Displacement Parameters for the Metal Atom Compositional Ordering Model of Type III Bi_3NbO_7 (Space group $I\bar{4}m2$ (no. 119), $a = 16.3180(2)$, $c = 38.5420(5)$ Å)

	x (a)	y (b)	z (c)	$100U_{iso}$ (Å^2)
Nb1	2/3	0	1/7	2.6(7)
Nb2	1/2	1/6	1/14	2.6(7)
Nb3	0	0	1/7	2.6(7)
Nb4	2/3	0	5/7	2.6(7)
Nb5	1/2	1/2	1/14	2.6(7)
Bi1	5/6	1/6	3/14	5.6(2)
Bi2	2/3	0	2/7	5.6(2)
Bi3	1/6	0	1/2	5.6(2)
Bi4	2/3	0	6/7	5.6(2)
Bi5	2/3	0	4/7	5.6(2)
Bi6	0	0	2/7	5.6(2)
Bi7	1/3	0	0	5.6(2)
Bi8	0	0	0	5.6(2)
Bi9	1/6	1/6	1/14	5.6(2)
Bi10	1/6	1/6	5/14	5.6(2)

Figs. 2*d* and 3*a*, it should be noted that pyrochlore-type itself can be constructed either from three $\langle 1\,1\,0\rangle_F$ strings, such as are found in Type II, or from two $\langle 1\,1\,0\rangle_F$ strings, such as are found in Type III. These two structures may therefore represent alternative expansions of pyrochlore-type for incorporation into fluorite-type, both based on a motif of $\langle 1\,1\,0\rangle_F$ strings of M atoms.

Bi_2O_3–WO_3 Type II

The Type II phase reported by Zhou (15) in the system Bi_2O_3–WO_3 as a solid solution in the range Bi_6WO_{12}–$Bi_{18}W_4O_{39}$ was identified (18) at approximately 17.5 mol% W_2O_6, and the reported tetragonal, $3\mathbf{a}_F$, $3\mathbf{b}_F$, $3\mathbf{c}_F$, F-centered superstructure of fluorite-type was confirmed.

Zhou inferred from HRTEM observations that W atoms were arranged on the $\langle 1\,1\,1\rangle \equiv \langle 1\,1\,1\rangle_F$ planes of this fluorite-type superstructure. In the context of the present study, this observation suggests that the structure may be related to those of Type II Bi_2O_3–$(Nb/Ta)_2O_5$, Type III Bi_3NbO_7, and $Bi_{38}Mo_7O_{78}$. These phases share a pyrochlore-type structural motif in the form of strings of MO_6 octahedra along $\langle 1\,1\,0\rangle_F$ directions (Fig. 3*d*). (The structure of Bi_2O_3–WO_3 Type II might, for example, be considered as a variant of Type II Bi_2O_3–$(Nb/Ta)_2O_5$ in which $\varepsilon = \frac{1}{3}$ (23).) Given the different expressions of the $\langle 1\,1\,0\rangle_F$ string motif in these structures, however, (Figs. 7–9) there are many possible models which could be proposed.

Any such proposals would need to be tested against observed diffraction data. Thus far, it has not been possible to obtain single-crystals of this phase, and neutron powder diffraction data have not been collected. Synchrotron XRD data display no significant intensity in the satellite reflections, indicating that there are no significant displacing relaxations of the metal atoms from their positions in the fluorite-type subcell, but providing no information about compositional ordering. The extremely small difference between the X-ray scattering powders of W and Bi atoms means that even with complete compositional ordering, the strongest modulation peaks would be less than 0.1% of the intensity of the $(1\,1\,1)_F$ peak. Therefore, given the available data, and in the absence of a definitive space-group determination from ED (18), a definitive structural model for this phase could not be proposed.

A structural model was proposed for this phase by Zhou (15) based on the cluster motif (Fig. 3c) for the inclusion of pyrochlore-type into fluorite-type (Fig. 2), and simulated HRTEM images and DPs were shown to agree with observations. The alternative string motif (Fig. 3d) might have a number of advantages in this case, such as allowing a higher symmetry (Zhou's model being monoclinic despite the metrically tetragonal cell) and a more flexible composition (Zhou's model having the composition $Bi_{46}W_8O_{93}$, i.e., 14.8 mol% W_2O_6). Ultimately, however, in the absence of useful diffraction data it can only be concluded that Bi_2O_3–WO_3 Type II is a superstructure of fluorite-type δ-Bi_2O_3, with very little displacing relaxation in the metal atom array.

Bi_2O_3–MoO_3 26:10

The structure of $Bi_{26}Mo_{10}O_{69}$ was solved and refined in a single-crystal X-ray study by Vannier *et al.* (29). This structure has been confirmed by Enjalbert *et al.* (30); however, these authors criticized the chemistry of Vannier *et al.* Enjalbert *et al.* disputed the existence of a phase with the reported structure type (isostructural with $Bi_{26}Mo_6V_4O_{67}$, also reported by Vannier *et al.* (29)) in the Bi_2O_3–MoO_3 system, suggesting that a small amount of alumina from the reaction vessel may have been responsible for stabilizing the structure by substituting for MoO_3. Vannier *et al.* subsequently reiterated their own conclusions (31), following a refinement of the structure of $Bi_{26}Mo_{10}O_{69}$ from neutron powder diffraction data (32) and noting the recent synthesis (18) of $Bi_{26}Mo_{10}O_{69}$ using sealed platinum tubing to remove the possibility of doping by impurities such as alumina.

The somewhat controversial chemistry of the phase has corresponded to slightly different interpretations of the details of the structure, in particular the location of the final oxygen atom. (Vannier *et al.*'s original structure was for $Bi_{26}Mo_{10}O_{68}$; the apparent oxygen overstoichiometry was the source of Enjalbert *et al.*'s criticisms.) Nonetheless, all reports are in agreement about the fundamental features of the structure, whereby $[Bi_{12}O_{14}]_\infty$ columns are surrounded by 10 MoO_4 tetrahedra organized in layers perpendicular

to [0 1 0], the layers being separated by an additional Bi atom between two tetrahedra. The structure in this sense bears strong relationships to the high-temperature structure of γ(H)–Bi_2MoO_6 (43). As stated previously (18), there appears to be little to gain from an interpretation of this structure type in terms of fluorite-type, despite the determination in that study of a relationship to a fluorite-type subcell. Despite using this fluorite-type parent structure to help determine their later model, Vannier *et al.* (31) agree with this conclusion. This model is shown in Fig. 10.

The principal reason for placing $Bi_{26}Mo_{10}O_{69}$ in a different category from other structures discussed in the present study, despite the fcc metal atom array, is the distribution and coordination environments of Mo atoms. Although

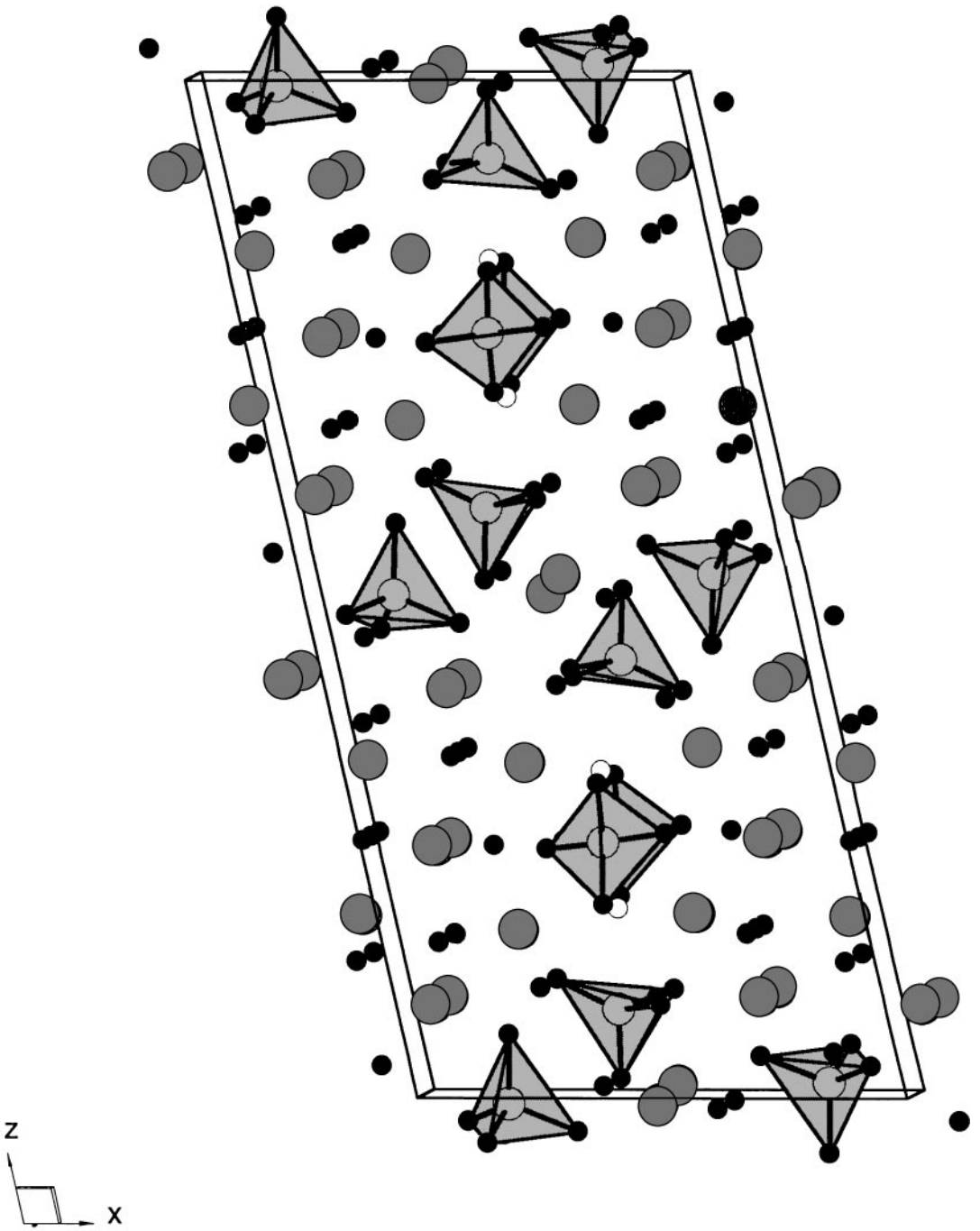

FIG. 10. The Rietveld-refined (neutron) structure of $Bi_{26.4}Mo_{9.6}O_{68.4}$ (31). Bismuth atoms are darker than molybdenum atoms and oxygen atoms are black. MoO_4 tetrahedra are shown.

isolated tetrahedral coordination environments were observed for Mo and W atoms in Type Ia $Bi_{14}(W/Mo)O_{24}$ (20), in that case the density of non-Bi atoms was too low to allow for extended connectivity between their coordination polyhedra. This is no longer so in the case of $Bi_{26}Mo_{10}O_{69}$. In other structures considered in this study, higher densities of non-Bi atoms have led to increasingly extensive connectivity between octahedral coordination environments, oriented along $\langle 1\,1\,0\rangle_F$ directions. Although $\langle 1\,1\,0\rangle_F$ connectivity can be found in $Bi_{26}Mo_{10}O_{69}$, no string extends further than one fluorite-type subcell, making comparisons with the continuous strings of pyrochlore-type (Fig. 2) highly tenuous. At the same time, the Mo_x clusters connecting these short strings bear no relationship to any clusters found in pyrochlore-type (Fig. 3), rendering the alternative cluster motif equally irrelevant to this structure. Any interpretation of the Mo distribution in $Bi_{26}Mo_{10}O_{69}$ in terms of pyrochlore-type structural motifs is therefore too contrived to be meaningful.

*Bi_2O_3–Ta_2O_5 Type II**

The structure of Type II* $Bi_7Ta_3O_{18}$ has recently been solved and refined using single-crystal synchrotron X-ray data (22), in conjunction with unit-cell and symmetry information derived from ED (18) (Fig. 11a). Space-group symmetry is triclinic $C1$ but is very close to monoclinic $C2/m$. The $C2/m$ prototype fitted all the Rietveld-refineable features of a medium-resolution, neutron powder diffraction pattern. The metal atom array is approximately fcc (fluorite-type), punctuated by regularly spaced displacement faults perpendicular to the $[1\,1\,1]_F$ direction every 2.5 fluorite unit cells. Ta atoms are octahedrally coordinated, with TaO_6 octahedra forming columns. The remaining oxygen atoms occupy distorted fluorite positions. Bi atoms occupy octahedral, square pyramidal, or trigonal prismatic sites within the oxygen array; strain in the latter coordination environment appears to be responsible for the lowering of symmetry from monoclinic to triclinic.

Although there were no unambiguous fluorite-type subcells in the diffraction patterns of Type II* $Bi_7Ta_3O_{18}$, a number of fluorite-like patterns were obtained in ED (see Fig. 7 of Ling *et al.* (18)). The origin of these patterns can be seen in the final refined structure. Figures 11b and 11c show only the metal atom array and clearly demonstrate the layered nature of the structure. Metal atoms between the layers have an fcc arrangement, highlighted by laying a fluorite-type grid over the metal atoms on either side (Fig. 11b). Fluorite-type slabs therefore exist continuously throughout the structure, except on the layers at $x = 0$ and $x = \frac{1}{2}$. Fluorite-type slabs are stepped on these planes, perpendicular to $[1\,1\,1]_F$ within the slabs, making it meaningless (and effectively impossible) to relate a unique, average fluorite-type subcell to the unit cell of $Bi_7Ta_3O_{18}$ in diffraction space. In terms of these slabs, the major projection shown in Fig. 11a is equivalent to $\langle 1\,1\,0\rangle_F$.

The nature of the $[1\,0\,0] \equiv \langle 1\,1\,1\rangle_F$ step itself can be seen in Figs. 11b and 11c. One of the metal atom layers perpendicular to $[1\,0\,0] \equiv \langle 1\,1\,1\rangle_F$ is repeated in the fcc stacking sequence along **a**, creating an approximately identical layer shifted by $\frac{1}{10}\mathbf{a}$, i.e., $\frac{1}{4}(\mathbf{a}_F + \mathbf{b}_F + \mathbf{c}_F)$. This introduces a primitive hexagonal double-layer into the stacking sequence of fluorite-type metal atom layers. This introduction of a primitive hexagonal double-layer is induced by corner-connection of TaO_6 octahedra perpendicular to the hexagonal close-packed metal atom layer (see Fig. 11a). Connection of TaO_6 octahedra in such a manner is incompatible with the maintenance of an fcc metal atom array. The fcc stacking sequence *–ABC–* of hexagonal layers is thereby expanded to *–ABCABBCABCCABCA–*. (Note that since the layers are shifted along **a**, the primitive double-layer is distorted slightly by the (pseudo)-monoclinic angle $\beta \sim 109^\circ$.)

Type II* $Bi_7Ta_3O_{18}$ can now be seen to contain $\langle 1\,1\,0\rangle_F$ strings of Ta atoms, the structural motif from pyrochlore-type (Fig. 3d) observed in many other phases investigated in this study. In this phase, strings are only found along one of the six possible $\langle 1\,1\,0\rangle_F$ directions and do not interact with each other within the fluorite-type slabs. The $\langle 1\,1\,0\rangle_F$ strings corner-connect across the primitive hexagonal step, but isolated strings do exist within the slabs. This robustness of the $\langle 1\,1\,0\rangle_F$ string structural motif across such different structures is a strong indication of its value in describing the structures of phases investigated in this study.

Bi_2O_3–Ta_2O_5 Type III

The structure of Type III $Bi_4Ta_2O_{11}$ has recently been solved and Rietveld-refined using neutron powder diffraction data (21). The structure is shown in Fig. 12. This phase is a close relative of the Type II* phase. The same continuous $\langle 1\,1\,0\rangle_F$ strings of Ta atoms, aligned along only one of the six $\langle 1\,1\,0\rangle_F$ directions, are in evidence. The fcc stacking sequence *–ABC–* of hexagonal layers is expanded by the interface modulation in much the same manner as that of Type II* $Bi_7Ta_3O_{18}$; in this case, to *–ABCCABBCA–*. In terms of this pyrochlore-type structural motif, an important distinction between the two structures is the absence of any truly isolated strings in Type III $Bi_4Ta_2O_{11}$; all are paired across primitive hexagonal steps. Consequently, any connection between Type III and a fluorite-type parent structure via a pyrochlore-type string motif, as discussed for Type II* $Bi_7Ta_3O_{18}$ and many other phases investigated in this study, is highly tenuous. Nonetheless, the obvious relationship between Bi_2O_3–Ta_2O_5 Types II* and III suggests that such a connection may have some (limited) meaning even for Type III $Bi_4Ta_2O_{11}$.

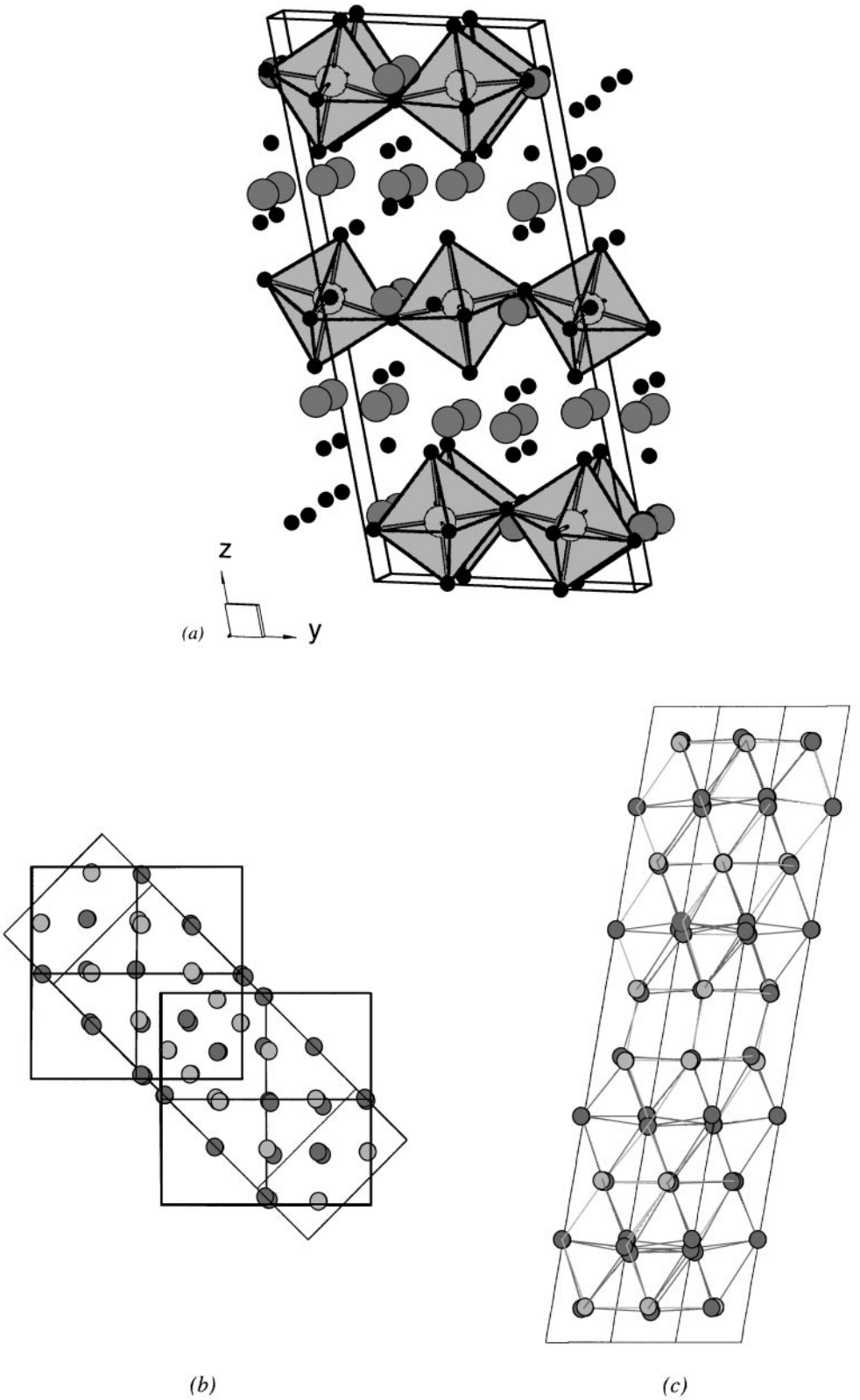

FIG. 11. (a) The single-crystal X-ray refined structure of Type II* $Bi_7Ta_3O_{18}$ (22). Bismuth atoms are darker than tantalum atoms and oxygen atoms are black. TaO_6 octahedra are shown. (b, c) The metal atom array viewed down the (b) $[\bar{1}\,0\,5] \equiv \langle 1\,0\,0\rangle_F$ and (c) $[0\,\bar{1}\,2] \equiv \langle 1\,1\,0\rangle_F$ directions. Dashed lines indicate a fluorite-type subcell grid. Nearest-neighbor metal atom connections are shown in (c).

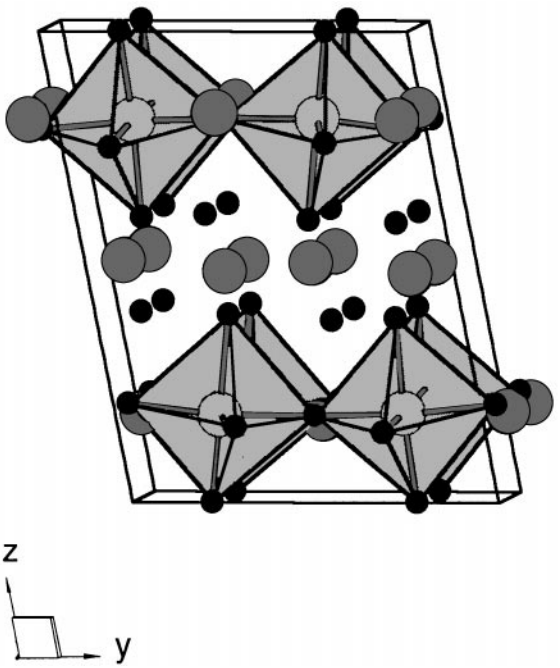

FIG. 12. The Rietveld-refined (neutron plus X-ray) structure of Type III $Bi_4Ta_2O_{11}$ (21). Bismuth atoms are darker than tantalum atoms and oxygen atoms are black. TaO_6 octahedra are shown.

Bi_2O_3–WO_3 and Bi_2O_3–MoO_3 n = 1 Aurivillius

Aurivillius phases (41, 42) are layered structures, consisting of perovskite-like $A_{n-1}B_nO_{3n+1}$ slabs regularly interleaved with α-PbO-like Bi_2O_2 layers. They share an *Fmmm* prototype parent structure (34). The $n = 1$ phases Bi_2WO_6 and Bi_2MoO_6 (25) can therefore be thought of as having planes of W/Mo atoms in a (distorted) fluorite-type metal atom array perpendicular to $[0\,0\,1]_F$. W/Mo atoms have octahedral coordination environments; therefore the planes can be thought of as $1 \times \infty \times \infty$ octahedra units of perovskite-type.

Bi_2O_3–Nb_2O_5 and Bi_2O_3–Ta_2O_5 Type IV

The prototype parent structure of Type IV $Bi_5Nb_3O_{17}$ has been shown to be more akin to perovskite-type than to fluorite-type δ-Bi_2O_3 (6, 8, 12, 18). Gopalakrishnan *et al.* (6) proposed a model based on an intergrowth between $n = 1$ and $n = 2$ members of the perovskite-related Aurivillius family of phases (33). In this model, the primary modulation wave-vector **q** (described by Ling *et al.* (18)) is ignored and only the parent structure is modeled. Gopalakrishnan *et al.* reported the long axis $c \sim 21$ Å, i.e., half the length observed by Zhou *et al.* (8, 12) and Ling *et al.* (18).

Zhou *et al.* proposed a more sophisticated model based on the $n = 1 + 2$ Aurivillius-type intergrowth concept. This model doubled the length of the long axis *c*, and also incorporated step-like dislocations observed in HRTEM as responsible for the **a*** component of **q** and approximated by Zhou *et al.* to a six-times supercell along **a**. It was possible to construct this model in the space group *B*1*m*1 (Fig. 13). In a recent study (19), testing against observed synchrotron XRD and neutron powder diffraction data showed the model of Zhou *et al.* to be more plausible than that of Gopalakrishnan *et al.*

Neither model provided a precise fit to observed data, particularly at high angle/low *d*-spacing. This is unsurprising given their high symmetry. Real Aurivillius-type phases are known to distort from idealized *Fmmm* parent structures via a series of rotational and displacing modes (34). The rotation of NbO_6 octahedra ought particularly to effect the neutron data, which is far more sensitive to oxygen atom displacements. Furthermore, even the large unit cell of Zhou *et al.*'s model is only an approximation to the incommensurate cell described recently (18).

Although this model appeared to have much in common with the true structure, Rietveld-refinements were unfortunately not feasible due to the large number of variables (216 independent atoms in *B*1), the relatively poor quality data, and the truly incommensurate nature of the unit cell. Given the high possibility of stacking faults in such a complex structure, and Zhou *et al.*'s observation (12) of a Type IV* variant on the same theme, it seems likely that the complexity of the true structure is such that a solution from powder diffraction data would be extremely difficult. At the same time, growth of single crystals of this phase remains elusive. HRTEM, used in the studies that proposed these models, is clearly a more appropriate technique, and the results presented here seem to vindicate their conclusion that the Type IV phase does not have a fluorite-type δ-Bi_2O_3-related parent structure in any meaningful sense.

Neither synchrotron XRD nor neutron powder diffraction data have been reported for the corresponding Type IV phase in the Bi_2O_3–Ta_2O_5 system, $Bi_{31}Ta_{17}O_{89}$. Zhou *et al.* (12) modeled the Type IV phase in the Bi_2O_3–Ta_2O_5 system, $Bi_{31}Ta_{17}O_{89}$, in essentially the same way as for $Bi_5Nb_3O_{17}$, based on an intergrowth between $n = 1$ and $n = 2$ Aurivillius phases, but with the step oriented in a different direction; this is in agreement with the different orientation of the primary modulation wave-vector **q** described recently (18). (The underlying similarity between these two phases is seen most clearly in Table 2 of Ling *et al.* (18).) In light of these similarities, the Type IV model of Zhou *et al.* for $Bi_{31}Ta_{17}O_{89}$ seems equally plausible as that proposed for $Bi_5Nb_3O_{17}$.

These phases can be thought of as having planes of Nb/Ta atoms in a fluorite-type metal atom array, arranged perpendicular to $[0\,0\,1]_F$ to create units of perovskite-type, as for the $n = 1$ Aurivillius phases. However, half of these planes interact with parallel planes to create $2 \times \infty \times \infty$ octahedra units of perovskite-type, as for $n = 2$ Aurivillius

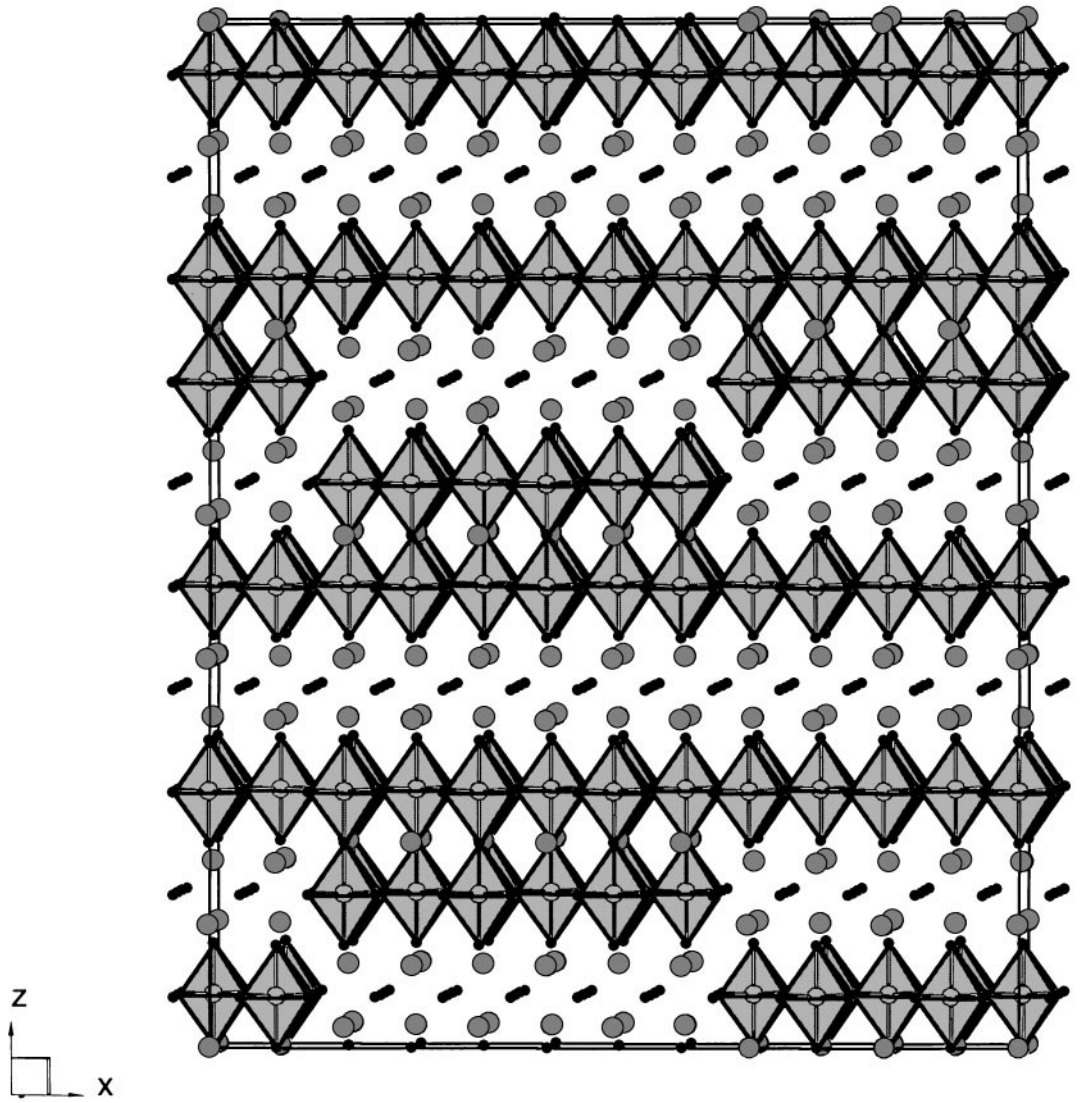

FIG. 13. The (unrefined) Aurivillius-type intergrowth model for Type IV $Bi_5Nb_3O_{15}$ (6, 19). Bismuth atoms are darker than niobium atoms and oxygen atoms are black. NbO_6 octahedra are shown.

phases, an interaction which does not occur in fluorite-type. It is this change in connectivity throughout the whole structure which clearly indicates that Bi_2O_3–$(Nb/Ta)_2O_5$ Type IV phases cannot be meaningfully be described in terms of a fluorite-type parent structure.

CRYSTAL-CHEMISTRY

Following the above summary, phases can now be grouped into five general types, those containing isolated *M* atoms (Bi_2O_3–Ta_2O_5 Type I; Bi_2O_3–MoO_3 Type Ia; Bi_2O_3–WO_3 Types Ia and Ib), $\langle 1\,1\,0\rangle_F$ strings of *M* atoms in three dimensions (Bi_2O_3–Nb_2O_5, –Ta_2O_5, and –WO_3 Type II), $\langle 1\,1\,0\rangle_F$ strings of *M* atoms in two dimensions (Bi_2O_3–Nb_2O_5 Type III; Bi_2O_3–MoO_3 38:7), $\langle 1\,1\,0\rangle_F$ strings of *M* atoms in one dimension (Bi_2O_3–Ta_2O_5 Types II* and III), and $\langle 1\,0\,0\rangle_F$ planes of *M* atoms (Bi_2O_3–Nb_2O_5 and –Ta_2O_5 Type IV; Bi_2O_3–WO_3 and –MoO_3 $n = 1$ Aurivillius). Bi_2O_3–MoO_3 26:10 does not fit any of these types.

Grouping phases according to these five categories and plotting them against composition (Fig. 14), it can be seen that there is a sequence of general types with increasing *M* presence in the metal atom array. Although the sequence is only truly valid within individual systems, and not all systems have a phase in each category, these variations are attributable to the different chemical characters of the *M* atoms, i.e., different preferred coordination environments for individual or groups of *M* atoms depending on *M*. Attention can then be focused on understanding, rather

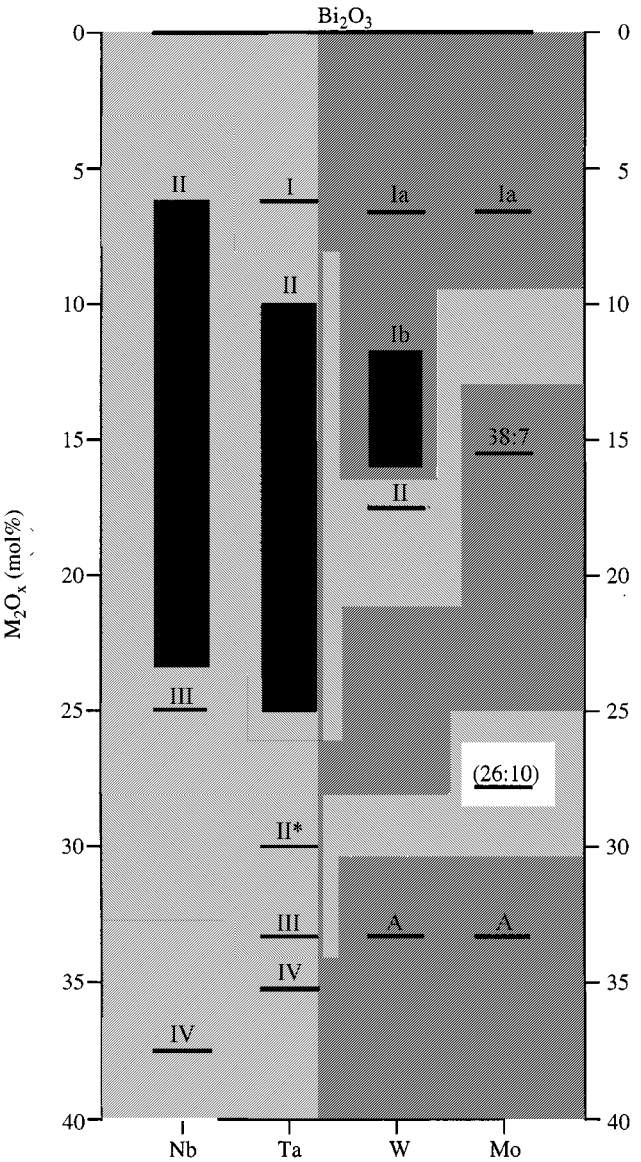

FIG. 14. Phases considered in this study, with respect to composition. Background shadings group phases with similar structural relationships to fluorite-type δ-Bi_2O_3.

than simply tabulating, the relationship between composition and structure type, i.e., the crystal–chemical relationship between these general types.

Figure 15 illustrates the observed patterns of M atom distribution mapped onto $3\times3\times3$ fluorite-type subcell grids, after the manner of the hypothetical pyrochlore-type $Bi_2M_2O_7$ shown in Fig. 2d mapped onto a $2\times2\times2$ fluorite-type subcell grid. Bi atoms and the fluorite-type subcell grid are omitted for clarity. (Note that the M ordering schemes shown for some of these structures, particularly Figs. 15a and 15c–15f), represent the preferred structural models but remain to be fully determined.) Isolated M atoms are seen in Figs. 15a–15c, strings of M atoms in three dimensions are seen in Fig. 15d, strings of M atoms in two dimensions are seen in Figs. 15e–15f, and strings of M atoms in one dimension are seen in Figs. 15g–15h.

Isolated M Atoms

Isolated M atoms are illustrated for the phases shown in Figs. 15a–15c. This is the simplest possible arrangement and clearly can accommodate the lowest M atom densities of any of the five structure types being discussed. As the M atoms are isolated from one another within the flexible oxygen atom array of fluorite-type δ-Bi_2O_3, they can adopt either octahedral (Bi_2O_3–Ta_2O_5 Type I; Bi_2O_3–WO_3 Type Ib) or tetrahedral (Bi_2O_3–$(W/Mo)O_3$ and Type Ia) coordination environments. Octahedral coordination is strongly favored by Ta^{5+} ions, but Mo^{6+} and W^{6+} ions can accommodate either coordination. The adoption of tetrahedral coordination environments in Type Ia allows the maximum number of disordered oxygen atom vacancies (25% of fluorite-type sites for pure δ-Bi_2O_3) to be constrained (in ordered positions) about W/Mo atoms. An isolated, tetrahedrally coordinated M atom constrains four fluorite-type oxygen vacancies (Fig. 16b). In the more WO_3-rich Type Ib, however, a shortage of oxygen atom vacancies forces W atoms to adopt octahedral coordination environments.

Interestingly, further increasing the concentration of M atoms in the metal atom array rapidly reduces the number of available oxygen vacancies, such that this structure type becomes unstable well before the theoretical maximum density of isolated M atoms within a fluorite-type Bi atom array (25%) is reached. M atoms begin to accumulate in $\langle1\,1\,0\rangle_F$ strings in order to reduce crowding in the oxygen atom array; if we assume octahedral coordination environments, an isolated M atom constrains two fluorite-type oxygen vacancies (Fig. 16c), whereas an M atom in a $\langle1\,1\,0\rangle_F$ string constrains only one (Fig. 16d).

Strings of M Atoms in Three Dimensions

Figure 15d shows M atoms aligned in three $\langle1\,1\,0\rangle_F$ strings at 60° to one another. The wide solid-solution ranges observed for this structure type in the Bi_2O_3–Nb_2O_5 and Bi_2O_3–Ta_2O_5 systems indicate that it is a particularly favorable configuration, due to the ability of the oxygen atom array to form strings of corner-connected MO_6 octahedra with only minor distortion from fluorite-type.

The maximum M atom density for this structure type is 50%, corresponding to a hypothetical pyrochlore-type $Bi_2M_2O_7$. Note that no such phase exists for M = Nb, Ta, W, or Mo, because charge balance would require M^{4+} ions; Nb^{5+}, Ta^{5+}, W^{6+}, and Mo^{6+} cations require more

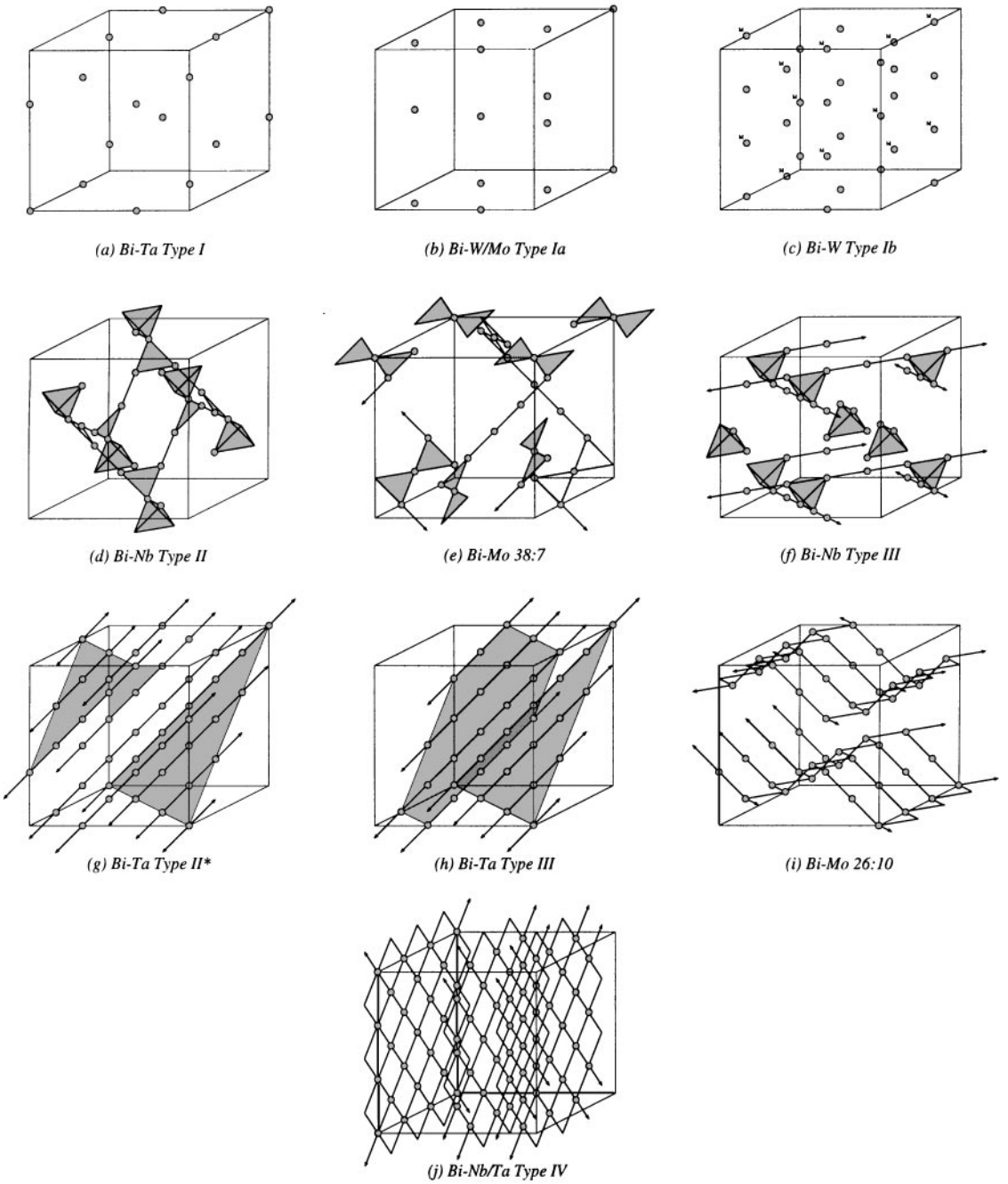

FIG. 15. Simplified representations of the structures of phases considered in this study, showing M atoms mapped onto $3 \times 3 \times 3$ fluorite-type subcells after the manner of Fig. 2d ($2 \times 2 \times 2$ fluorite-type subcells). Nearest-neighbor connectivity is shown as lines, triangles, and tetrahedra. Mixed occupancy sites are labeled "M" in (c). Shaded planes represent the boundaries of fluorite-type slabs in (g) and (h).

O^{2-} anions than can fit into ideal pyrochlore-type. The fact that this structure type is far more stable in the Bi_2O_3–Nb_2O_5 and Bi_2O_3–Ta_2O_5 systems than in the Bi_2O_3–WO_3 and Bi_2O_3–MoO_3 systems can be explained in terms of M^{5+} ions causing less crowding in the oxygen atom array than M^{6+} ions. Similarly, charge-balance explains why this structure type ceases to be the most stable option well before reaching the hypothetical maximum M atom density of 50%, i.e., pyrochlore-type $Bi_2M_2O_7$ (Fig. 2d).

Strings of M Atoms in Two Dimensions

The structures shown in Figs. 15e and 15f contain M atoms aligned in two perpendicular $\langle 1\,1\,0 \rangle_F$ strings,

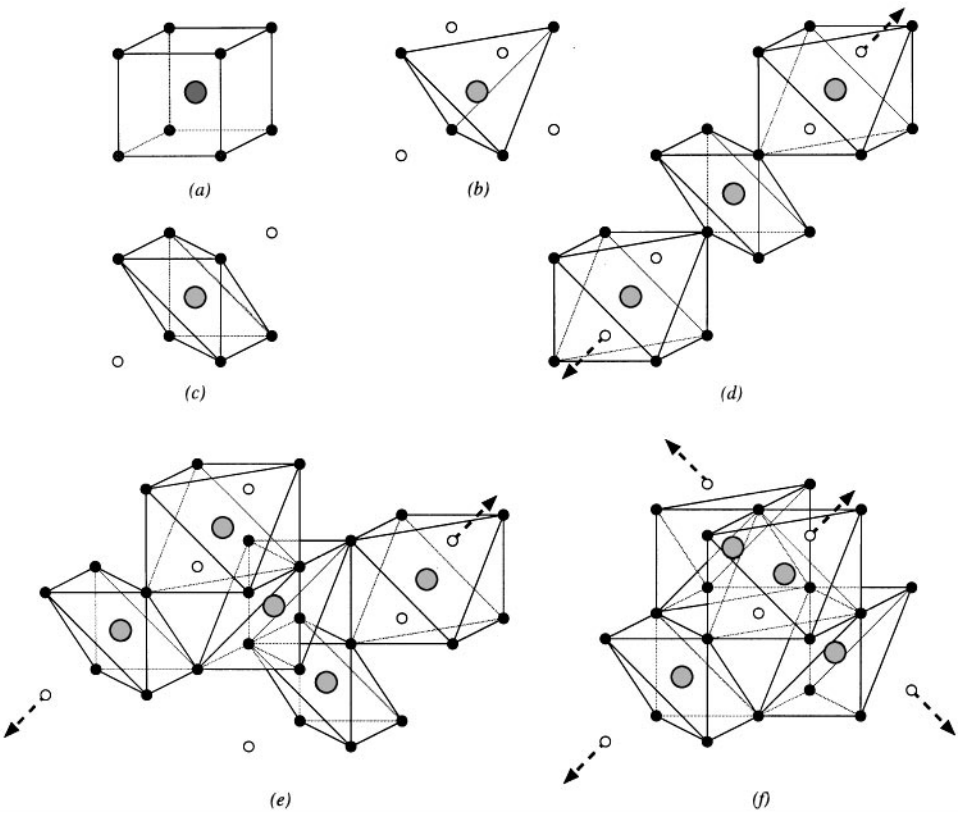

FIG. 16. (a) The disordered fluorite-type oxygen atom array of δ-Bi_2O_3. This is compared to the fluorite-type oxygen vacancy ordering patterns which follow from isolated, tetrahedrally coordinated M atoms (b) and octahedrally coordinated M atoms when (c) isolated, (d) in $\langle 1\ 1\ 0\rangle_F$ strings, (e) in M_5 triangular clusters on stepped $\langle 1\,1\,0\rangle_F$ strings, and (f) in tetrahedral clusters where perpendicular $\langle 1\,1\,0\rangle_F$ strings interact. Bi atoms are darker than M atoms, oxygen atoms are black, oxygen vacancies are white, and 75% occupied oxygen sites are striped. Dashed arrows indicate that the $\langle 1\,1\,0\rangle_F$ string continues; i.e., the oxygen vacancy is shared with an adjacent M atom. Oxygen atom displacements from fluorite-type are not shown.

which can interact (as in Type III Bi_3NbO_7) and may be stepped (as in $Bi_{38}Mo_7O_{78}$). As for the Type II structures, this has the effect of reducing the M:Bi ratio in hypothetical $Bi_2M_2O_7$ pyrochlore to the point at which charge-balance considerations allow it to exist. In pyrochlore-type, all six $\langle 1\,1\,0\rangle_F$ strings of M atoms are present. In the Type II phases (Fig. 15d), the network of strings is expanded around an M atom, leaving a set of three strings at 60° to one another, each perpendicular to a different $\langle 1\,0\,0\rangle_F$ direction (e.g., $[1\,1\,0]_F$, $[1\,0\,1]_F$, and $[0\,1\,1]_F$). In the structures shown in Figs. 15e and 15f, the network of strings is expanded around the center of an MO_4 tetrahedron, leaving a pair of strings at 90° to one another, perpendicular to the same $\langle 1\,0\,0\rangle_F$ direction. These general structure types are nonetheless closely related, the transition between Bi_2O_3–Nb_2O_5 Types II and III having been discussed previously (18) in terms of their relationships on the level of space-group symmetry and DPs.

The fact that this structure type (III) is more niobium-rich than Type II in the Bi_2O_3–Nb_2O_5 system, and that it is observed in the Bi_2O_3–MoO_3 system whereas a Type II phase is not, suggests that it is a more successful adaptation of pyrochlore-type in terms of overcoming charge-balance problems. This is due to the increased concentration of M atoms in Nb_4 tetrahedral clusters where perpendicular strings come into contact (Type III Bi_3NbO_7) and the triangular pattern of Mo_5 clusters where the strings are stepped ($Bi_{38}Mo_7O_{78}$). With fewer independent string directions, there are more of these clusters for a given length of string. The former construction reduces oxygen crowding more effectively than strings (one fluorite-type oxygen vacancy constrained per M atom); each M atom in an M_4 tetrahedral cluster on a string (Fig. 16f) is associated with 3/4 fluorite-type oxygen vacancies. The driving force behind the formation of Type III Bi_3NbO_7 is therefore charge balance. Each M atom in the latter construction, an M_5 triangular cluster on a string (Fig. 16e), is associated with one fluorite-type oxygen vacancy. Consequently, the driving force behind the formation of $Bi_{38}Mo_7O_{78}$ is less clear and may simply reflect an inherent stability in these clusters.

Strings of M Atoms in One Dimension

The M atoms in the Bi_2O_3–Ta_2O_5 Type II* and III structures shown in Figs. 15g and 15h are aligned in strings along a single $\langle 1\,1\,0\rangle_F$ direction. In this sense, the structure type is a logical progression, and the structural relationship to the previous general types seems clear. The crystal–chemical progression in terms of oxygen crowding also seems obvious; aligned in strings parallel and adjacent to other strings, each M atom constrains only 1/2 fluorite-type oxygen vacancies. On closer examination of the structures, however, it emerges that these units are not in fact pairs of adjacent $\langle 1\,1\,0\rangle_F$ strings. In terms of a fluorite-type metal atom array, the strings are moved within contact distance via an interface modulation layer perpendicular to $\langle 1\,1\,1\rangle_F$. The fcc stacking sequence of hexagonal layers $-ABC-$ is thereby stepped between layers, creating primitive hexagonal double-layers and hence the overall sequences $-ABCABBCABCCABCA-$ (Type II* $Bi_7Ta_3O_{18}$) or $-ABCCABBCA-$ (Type III $Bi_7Ta_3O_{18}$).

This structure type therefore represents the abandonment of (fcc) pyrochlore-type structural motifs alone to accommodate M atoms into the fluorite-type metal atom array. This significant change in structure type is driven by charge balance, i.e., the shortage of oxygen vacancies in the pure fluorite-type array at these compositions.

Planes of M Atoms

Figures 15i and 15j show structure types that are clearly unrelated to pyrochlore-type despite the fact that they can be mapped onto fcc metal atom arrays. Figure 15i Shows the buckled $\langle 1\,0\,0\rangle_F$ M atom planes of $Bi_{26}Mo_{10}O_{69}$ which, as discussed in Structural Models, above, contains none of the structural motifs from pyrochlore-type shown in Figs. 3b–3d. This structure type therefore provides no link between fluorite-type and pyrochlore-type.

In Fig. 15j, the obvious $\langle 1\,0\,0\rangle_F$ planes of M atoms could be interpreted as an infinite series of adjacent parallel (or criss-crossing) $\langle 1\,1\,0\rangle_F$ strings; however, the fact that $\langle 1\,1\,0\rangle_F$ strings are never adjacent and never cross one another in pyrochlore-type (Fig. 2) means that no useful analogy can be made. The planes thus formed are in fact of perovskite-type, separated by Bi-only layers as in Aurivillius-type structures. The oxygen atom array accompanying this metal atom array no longer bears any relationship to fluorite-type. The driving force behind the adoption of this general structure-type at M_2O_x-rich compositions in all the systems studied (Bi_2O_3–$(Nb/Ta)_2O_5$ Type IV and $Bi_2(W/Mo)O_6$ Aurivillius) is that there are insufficient vacancies available in a fluorite-type oxygen atom array for the accommodation of octahedrally coordinated M atoms, regardless of M atom configuration.

It is important to realize that this general structure type does not represent a progression from the previous one, either structurally or crystal-chemically. The crystal–chemical scheme used to unify the structural types discussed so far breaks down at these M_2O_x-rich compositions, descriptions of which are therefore beyond the scope of the present study. None of the phases investigated in this study with greater than 25 mol% M_2O_x really fit this crystal–chemical scheme.

DISCUSSION

The general crystal–chemical scheme describing the phases considered in this study can be summarized as follows. Starting with fluorite-type δ-Bi_2O_3, which has 25% fluorite-type oxygen vacancies and highly flexible coordination environments for all metal atoms, 5 + and 6 + valent cations are substituted for Bi^{3+}. The number of available fluorite-type oxygen vacancies subsequently decreases, while at the same time, the need for these vacancies to satisfy the relatively rigid coordination environments of M atoms increases. The interaction between these competing structural influences is the driving force behind the general structure type adopted. Up to approximately 25 mol% M_2O_x, it is possible to accommodate the M atoms and associated change in vacancy concentration with pyrochlore-type structural motifs while preserving the fcc metal atom array of fluorite-type. At more M_2O_x-rich compositions, however, pyrochlore-type motifs alone are no longer feasible and it is necessary to abandon the fluorite-type δ-Bi_2O_3-related average subcell in favor of a variety of different structural types.

The key observation arising from this is the fact that, although structural types are defined by compositional ordering in the fluorite-type metal atom array (Fig. 15), the driving force behind the adoption of one or another type at a given stoichiometry is the compositional (i.e., vacancy) ordering within the fluorite-type oxygen atom array (Fig. 16).

The importance of satisfying the oxygen atom array also guides many of the models proposed by Zhou *et al.* (8–10, 12, 14–16) in the same systems. These authors also use the transition from fluorite-type to pyrochlore-type as a means of preserving a fluorite-type δ-Bi_2O_3-related subcell in Bi_2O_3-rich phases, and abandon it at more M_2O_x-rich compositions (although, due to some misinterpreted DPs in the Bi_2O_3–Ta_2O_5 system (18), they abandon it at slightly more M_2O_x-rich compositions). The important distinction between the approach of Zhou *et al.* and that of the present study is the emphasis by the former on tetrahedral clusters of MO_6 octahedra and by the latter on $\langle 1\,1\,0\rangle_F$ strings of MO_6 octahedra as the key structural motif from pyrochlore-type. Although there is some crossover between these motifs, the different approaches have led to different

structural models or solutions for all but the most Bi_2O_3-rich of the fluorite-type δ-Bi_2O_3-related phases (those with isolated M atoms).

In addition to the structural evidence considered in this study, a further argument against the approach of Zhou *et al.* is found in the driving forces behind transitions between structure types, as discussed above. Each M atom in an isolated M_4 tetrahedral cluster (Fig. 16f without the arrows) constrains 5/4 fluorite-type oxygen vacancies, more than an M atom in a $\langle 1\,1\,0\rangle_F$ string (which constrains only one). Isolated clusters such as this are therefore a less effective means of incorporating MO_6 octahedra into fluorite-type in the face of the competing charge-balance interaction. Each M_4 tetrahedral cluster would have to be connected to at least two others in order to achieve one fluorite-type oxygen vacancy per M atom.

Throughout this study the notation of Zhou *et al.* with regard to general structural types has been employed for the sake of clarity. From Fig. 14, it can be seen that this notation is largely, but not entirely, in agreement with the results of the present study. Certainly the phases labeled Type I/Ia/Ib and Type II are grouped in agreement with the present study. Present results also agree that Bi_2O_3–Nb_2O_5 Type III is a separate general type and suggest that $Bi_{38}Mo_7O_{78}$ could reasonably be referred to as Type III*. The labeling of Bi_2O_3–Ta_2O_5 Types II* and III is, however, quite inappropriate. Given that Type IV refers to a further, independent, general structure type, it might be more appropriate to refer to these phases ($Bi_7Ta_3O_{18}$ and $Bi_4Ta_2O_{11}$) as Type V. However, since the phases in question have been demonstrated to have fully ordered structures largely independent of fluorite-type, it seems unlikely that they will henceforth be referred to in terms of an average fluorite-type parent structure.

Figure 14 indicates that despite the existence of parallel trends in each system, the individual chemical characters of the M cations play a significant role in determining the structure type adopted. Clearly the differences between the pairs W^{6+}/Mo^{6+} and Nb^{5+}/Ta^{5+} are the greatest; therefore valence state is far more significant than atomic weight (i.e., cation size). This reflects the importance of charge balance in the crystal–chemistry of these phases, as discussed above. As expected, pyrochlore-type structural motifs can be incorporated into a fluorite-type average structure at much higher M^{5+} than M^{6+} concentrations. The role of cation size in determining structure type is subtler and cannot be explained in terms of the general crystal–chemistry of these systems.

An important test of the proposed crystal–chemical scheme is to relate it to the bismuth-rich regions of the phase diagrams of other Bi_2O_3–M_2O_x systems. First, it is expected that the valence of M will play an important role. In particular, systems where the valence is $3+$ or less will not be subject to the charge balance considerations which comprise one of the two competing interactions described in this study; such systems would therefore be expected to exhibit quite different behavior, potentially preserving a fluorite-type δ-Bi_2O_3-related structure at much higher MO_x concentrations. This is borne out in, e.g., the system Bi_2O_3–Y_2O_3, in which one fcc superstructure phase is reported to be stable from $25 \sim 43$ mol% Y_2O_3 (35) and another from 47.5–49 mol% Y_2O_3 (36).

Bi_2O_3–M_2O_x systems where M has a $5+$ or $6+$ valence would be expected to exhibit similar behavior to those investigated in the present study. Perhaps the most interesting case in point is the Bi_2O_3–V_2O_5 system, investigated in a range of studies (11, 13, 17, 37, 38). Structural types found in the bismuth-rich part of the phase diagram of this system appear to be broadly consistent with those found in the other systems described in this study. Phases labeled Types I and II(a–f) by Zhou (11, 13), e.g., clearly possess comparable modulations of fluorite-type δ-Bi_2O_3 in comparable compositional ranges.

In a recent exploratory investigation (39), the behavior of the Bi_2O_3–V_2O_5 system could not be comprehensively documented due to problems controlling the valence state of V. It appears that the reduction of V^{5+} to V^{4+} adds an additional degree of freedom to this system (40). This may have some bearing on the plethora of δ-Bi_2O_3-related phases reported by Zhou (11, 13) (Types I ($Bi_{50}V_4O_{85}$), IIa ($Bi_{46}V_8O_{89}$), IIb ($Bi_{46}V_8O_{89}$), IIc ($Bi_{46}V_8O_{89}$), IId ($Bi_{31}V_5O_{59}$), IIe (Bi_7VO_{13}), and IIf ($Bi_{43}V_{11}O_{92}$); it is possible that different reported phases at the same composition represent different net oxidation states of V in individual crystallites examined by TEM. More exotic synthetic methods are probably needed to control reduction in this system, as suggested by the recent study of Pang *et al.* (17), in which hydrothermal and solid-state synthetic routes produced completely different phases at approximately the same composition.

If sufficient control could be achieved over the valence state of V, it would be interesting to reinvestigate the bismuth-rich part of the Bi_2O_3–V_2O_5 system in the context of the crystal–chemical scheme proposed in this study. Models proposed by Zhou for the Types II(a–f) phases are of particular interest, as they are based on tetrahedral clusters, rather than $\langle 1\,1\,0\rangle_F$ strings, of V atoms in a fluorite-type metal atom array, i.e., the alternative pyrochlore-type structural motif. The reduction of V^{5+} would make the system even more interesting in terms of the proposed crystal–chemical importance of the valence of M. With mixed valence as an option, the valence states presumably would be stabilized by the structure; i.e., there would be an additional variable that would allow more complex metal atom arrangements, e.g., $Bi^{3+}/V^{5+}/V^{4+}$ ordering, potentially stabilizing a fluorite-type δ-Bi_2O_3-related average structure at higher V_2O_5 concentrations.

CONCLUSION

The central goal of this study has been to achieve an understanding of the crystal-chemistry unifying the fundamental structural features of the pseudo-binary systems Bi_2O_3–Nb_2O_5, Bi_2O_3–Ta_2O_5, Bi_2O_3–WO_3, and Bi_2O_3–MoO_3. The scheme proposed is based around the transformation of a fluorite-type structure via the incorporation of a pyrochlore-type structural motif of strings of M atoms along $\langle 1\,1\,0 \rangle_F$ directions. The orientations of these strings and the way they interact are driven by the competing requirements of overall charge-balance (hence composition) and local coordination environment within a modulated fluorite-type oxygen atom array. These interactions link the oxygen atom array to the metal atom array, and both to composition. At very Bi_2O_3-rich compositions, where insufficient M atoms are available to form viable strings, the coordination environments of isolated M atoms are likewise determined by the interplay between charge balance and preferred coordination environment. At more M_2O_x-rich compositions, it is this interaction among composition, oxygen atom array, and metal atom array which forces the eventual abandonment of this pyrochlore-type motif, and hence of any meaningful relationship to a fluorite-type δ-Bi_2O_3-related parent structure.

It is interesting to note that the reason such a wide variety of structure types are observed in these systems is the same reason for which these systems have come to the attention of researchers, the inherent flexibility of the coordination environment for Bi atoms in δ-Bi_2O_3. This flexibility is the source of the very high anionic conductivity observed in δ-Bi_2O_3 itself and in fluorite-type δ-Bi_2O_3-related phases, and it allows the more rigid coordination environments preferred by certain transition metals to be accommodated within the fluorite-type lattice. The results of the most complete structure determinations (20–22) provide further evidence that the bond valence requirement of Bi^{3+} is capable of being satisfied by 5-, 6-, 7-, or 8-fold oxygen coordinations.

Further work will be necessary to confirm the proposed crystal–chemical scheme. To this end, more crystal structure information will be needed from the systems studied. This may be achieved by growing single-crystals from phases that defied all attempts in the present study by using more exotic crystal growth techniques, e.g., fluxes, to allow very low temperature growth of crystals below possible displacing phase transitions and thereby obtaining useable single domain crystals. The use of high pressure could also be explored. Where growth of single-crystals continues to prove impossible, emerging *ab initio* structural modeling techniques using powder diffraction data may eventually be able to extend the achievements of the present study.

This study could also be extended in terms of the range of systems covered. Bi_2O_3–M_2O_x systems have been subject to a large number of investigations for a large range of M (and of x). Now that a general crystal–chemical scheme has been proposed to describe the structural behavior of bismuth-rich phases when M = Nb, Ta, Mo, and W, it is necessary to test the generality of this scheme against other, possibly analogous, systems. Preliminary investigations into the most obvious such system, Bi_2O_3–V_2O_5, indicated the need for more exotic synthetic techniques (beyond the scope of this study) to control the suspected reduction of V^{5+}. Many other systems are reported to possess bismuth-rich phases with underlying average fcc (i.e., fluorite-type) metal atom arrays. The ability or otherwise of the crystal–chemical scheme proposed here to be adapted or extended to these systems, as the structures of relevant phases are more accurately determined, will be a crucial test of the usefulness of the conclusions of this study.

REFERENCES

1. T. Takahashi and H. Iwahara, *Mater. Res. Bull.* **13,** 1447 (1978).
2. A. W. Sleight, *Science* **208** (4446), 895 (1980).
3. G. Gattow and H. Schröder, *Z. Anorg. Allg. Chem.* **318,** 176 (1962).
4. H. A. Harwig, *Z. Anorg. Allg. Chem.* **444,** 151 (1978).
5. P. D. Battle, C. R. A. Catlow, J. Drennan, and A. D. Murray, *J. Phys. C Solid State Phys.* **16,** L561 (1983).
6. J. Gopalakrishnan, A. Ramanan, C. N. R. Rao, D. A. Jefferson, and D. J. Smith, *J. Solid State Chem.* **55,** 101 (1984).
7. D. J. Buttrey, D. A. Jefferson, and J. M. Thomas, *Mater. Res. Bull.* **21,** 739 (1986).
8. W. Zhou, D. A. Jefferson, and J. M. Thomas, *Proc. R. Soc. London Ser. A* **406,** 173 (1986).
9. W. Zhou, D. A. Jefferson, and J. M. Thomas, *J. Solid State Chem.* **70,** 129 (1987).
10. W. Zhou, D. A. Jefferson, M. Alario-Franco, and J. M. Thomas, *J. Phys. Chem.* **91,** 512 (1987).
11. W. Zhou, *J. Solid State Chem.* **76,** 290 (1988).
12. W. Zhou, D. A. Jefferson, and J. M. Thomas, *Geophys. Monogr.* **43,** 113 (1989).
13. W. Zhou, *J. Solid State Chem.* **87,** 44 (1990).
14. W. Zhou, *J. Solid State Chem.* **101,** 1 (1992).
15. W. Zhou, *J. Solid State Chem.* **108,** 381 (1994).
16. D. Tang and W. Zhou, *J. Solid State Chem.* **119,** 311 (1995).
17. G. Pang, S. Feng, Y. Tang, C. Tan, and R. Xu, *Chem. Mater.* **10,** 2446 (1998).
18. C. D. Ling, R. L. Withers, S. Schmid, and J. G. Thompson, *J. Solid State Chem.* **137,** 42 (1998).
19. C. D. Ling, Ph.D. Thesis, Chap. 4, Australian National University, Canberra, Australia, submitted for examination.
20. C. D. Ling, R. L. Withers, J. G. Thompson, and S. Schmid, *Acta Crystallogr. B* **55,** 306 (1999).
21. C. D. Ling, J. G. Thompson, R. L. Withers, and S. Schmid, *J. Solid State Chem.* **142,** 33 (1999).
22. C. D. Ling, S. Schmid, R. L. Withers, J. G. Thompson, N. Ishizawa, and S. Kishimoto, *Acta Crystallogr. B* **55,** 157.
23. R. L. Withers, C. D. Ling, and S. Schmid, *Z. Krist.* **214**(5), 296 (1999).
24. O. Savborg and M. Lundberg, *J. Solid State Chem.* **57,** 135 (1985).
25. J. G. Thompson, S. Schmid, R. L. Withers, A. D. Rae, and J. D. Fitzgerald, *J. Solid State Chem.* **101,** 309 (1992).

26. A. Watanabe, N. Ishizawa, and M. Kato, *J. Solid State Chem.* **60,** 252 (1985).
27. L. Berg, G. Czack, V. Haase, H. Hein, H. Katscher, G. Kirchstein, H. K. Kugler, and S. Ruprecht, Eds., "Gmelin Handbuch der Anorganischen Chemie," Vol. W Erg.–Bd B 2, Sect. 3.2.11, p. 74. Springer-Verlag, Berlin, 1979.
28. A. Castro, E. Aguado, J. M. Rojo, P. Herrero, R. Enjalbert, and J. Galy, *Mater. Res. Bull.* **33,** 31 (1998).
29. R. N. Vannier, G. Nowogrocki, G. Mairesse, and F. Abraham, *J. Solid State Chem.* **122,** 394 (1996).
30. R. Enjalbert, G. Hasselmann, and J. Galy, *J. Solid State Chem.* **131,** 236 (1997).
31. R. N. Vannier, F. Abraham, G. Nowogrocki, and G. Mairesse, *J. Solid State Chem.* **142,** 294 (1999).
32. D. J. Buttrey, T. Vogt, G. P. A. Yap, and A. L. Rheingold, *Mater. Res. Bull.* **32,** 947 (1997).
33. B. Aurivillius, *Arkiv. Kemi.* **2,** 519 (1950).
34. R. L. Withers, J. G. Thompson, and A. D. Rae, *J. Solid State Chem.* **94,** 404 (1991).
35. T. Takahashi, H. Iwahara, and T. Arao, *J. Appl. Electrochem.* **5,** 187 (1975).
36. A. Watanabe, *J. Solid State Chem.* **124,** 287 (1996).
37. S. Kashida and T. Hori, *J. Solid State Chem.* **122,** 358 (1995).
38. V. F. Katkov, I. V. Pruzhko, and A. K. Kushnereva, *Inorg. Mater.* **33,** 481 (1997).
39. C. D. Ling, Ph.D. Thesis, Chap. 3, Australian National University, Canberra, Australia, submitted for examination.
40. M. Huvé, R.-N. Vannier, G. Nowogrocki, G. Mairesse, and G. V. Tendeloo, *J. Mater. Chem.* **6,** 1339 (1996).
41. B. Aurivillius, *Arkiv. Kemi.* **1,** 463 (1949).
42. B. Aurivillius, *Arkiv. Kemi.* **2,** 519 (1951).
43. D. J. Buttrey, T. Vogt, U. Wildgruber, and W. R. Robinson, *J. Solid State Chem.* **111,** 118 (1994).